Thin Solid Films 520 (2012) 5097–5122

Contents lists available at SciVerse ScienceDirect

Thin Solid Films

journal homepage: www.elsevier.com/locate/tsf

Critical review

Thin film metallic glasses: Unique properties and potential applications

Jinn P. Chu [a,*], J.S.C. Jang [b], J.C. Huang [c], H.S. Chou [c], Y. Yang [d], J.C. Ye [d], Y.C. Wang [e], J.W. Lee [f], F.X. Liu [g], P.K. Liaw [g], Y.C. Chen [h], C.M. Lee [h], C.L. Li [h], Cut Rullyani [a]

[a] Department of Materials Science and Engineering, National Taiwan University of Science and Technology, Taipei, 10607, Taiwan
[b] Institute of Materials Science and Engineering, Department of Mechanical Engineering, National Central University, Chung-Li, 32001, Taiwan
[c] Department of Materials and Optoelectronic Science, National Sun Yat-Sen University, Kaohsiung, 80424, Taiwan
[d] Department of Mechanical Engineering, The Hong Kong Polytechnic University, Hung Hom, Kowloon, Hong Kong
[e] Department of Civil Engineering, National Cheng Kung University, Tainan, 70101, Taiwan
[f] Department of Materials Engineering, Ming Chi University of Technology, New Taipei City 24301, Taiwan
[g] Department of Materials Science and Engineering, University of Tennessee, Knoxville, TN 37996-2200, USA
[h] Graduate Institute of Applied Science and Technology, National Taiwan University of Science and Technology, Taipei, 10607, Taiwan

ARTICLE INFO

Article history:
Received 21 March 2012
Accepted 22 March 2012
Available online 9 April 2012

Keywords:
Metallic glass
Amorphous
Solid-state amorphization
Microcompression
Adhesion
Wear resistance

ABSTRACT

A new group of thin film metallic glasses (TFMGs) have been reported to exhibit properties different from conventional crystalline metal films, though their bulk forms are already well-known for high strength and toughness, large elastic limits, and excellent corrosion and wear resistance because of their amorphous structure. In recent decades, bulk metallic glasses have gained a great deal of interest due to substantial improvements in specimen sizes. In contrast, much less attention has been devoted to TFMGs, despite the fact that they have many properties and characteristics, which are not readily achievable with other types of metallic or oxide films. Nevertheless, TFMGs have been progressively used for engineering applications and, thus, deserve to be recognized in the field of thin film coatings. This article will thus discuss both properties and applications of TFMGs including a review of solid-state amorphization upon annealing, the glass-forming ability improvement due to thin film deposition, and mechanical properties, including residual stress, hardness and microcompression, adhesion, and wear resistance. Potential applications and simulations will also be discussed.

Contents

* Corresponding author.
E-mail address: jpchu@mail.ntust.edu.tw (J.P. Chu).

0040-6090/$ – see front matter © 2012 Elsevier B.V. All rights reserved.
doi:10.1016/j.tsf.2012.03.092

List of symbols

β	taper angle
γ	weighting factor
ξ	effective hopping integer
σ_f	residual stress in the film
δ	total displacement
δ_i	initial depth of blade indentation
ρ	radius of curvature
ΔT	supercooled liquid region, SCLR
a	effective contact radius
A, p, q	system-specific parameters for molecular-dynamics simulations
dx	increment of blade displacement
D	diameter of micropillar
e	electron charge
exp	exponential function
E_r	reduced 'composite' modulus of the film/substrate system
E_{si}	Young's modulus of Silicon
E_i	Young's modulus of the diamond indenter
E_f	Young's modulus of film
E_s	Young's modulus of substrate
f	dimensionless function
F	applied force
h	indentation depth
H	height of micropillar
l	length of cut surface
L_f	Firsov screening length
J_{Ic}	Mode I fracture toughness
M_s	substrate biaxial modulus
P	applied load
r_i	distance between two atoms, i and j
r_0	first-neighbor distance
R_0	radii of curvatures of the substrate before film deposition
R	radii of curvatures of the substrate after the film deposition
t_s	substrate thickness
t_f	film thickness
T_g	glass transition temperature
T_x	crystallization temperature
ν	Poisson's ratio
ν_i	Poisson's ratio of the diamond indenter
ν_f	Poisson's ratio of film
ν_s	Poisson's ratio of substrate
V_{ij}	pair-wise Moliére potential
Z_1	ion gas atomic number
Z_2	neutral atom atomic number

1. Introduction

Metallic glasses (MGs), or amorphous metallic alloys, are non-crystalline metals which lack long-range atomic periodicity because they are generally formed with fast quench rates for the retention of the glassy state from the melt. MGs are non-equilibrium materials; important characteristics are the glass transition and crystallization temperatures when heated toward the liquid state. Due to the disordered atomic structure and the absence of grain boundaries, MGs have many superior properties including good soft-magnetic properties and excellent mechanical properties of high specific strength, large elastic limits (~2%), and high resistance to corrosion and wear. Thus, they have been a subject of interest for scientific research and engineering application for decades. The pioneering work by Klement et al. [1], Chen and Turnbull [2], and Chen [3] in the 1960s and 1970s reported the first MG samples based upon binary Au – Si and ternary Pd – Si – X (X═Ag, Cu or Au), and Pd – Y – Si (Y═Ni, Co or Fe) systems, using rapid solidification methods such as splat quenching. MGs at that time were limited to relatively small sizes, typically of order μm, in order to achieve fast quench rates. The recent advent of MGs with relatively high thermal stability and low critical cooling rates, primarily through multi-component composition design, has led to significant improvements in characteristic specimen sizes (thickness and diameter). As a result, many MGs (*e.g.* Zr-, Cu-, Ti-, Fe-, Pd-, Pt- and Au-based systems) with sizes in excess of 1 mm ("bulk" metallic glasses, BMGs) have been reported [4]. These BMG systems generally have good glass-forming ability (GFA) such that rapid solidification is unnecessary and BMGs thus have become obtainable with conventional copper-mold casting methods.

Increasing interest in developing and understanding this new family of materials has also led to making thin film metallic glass (TFMG) processing possible, which was not readily achieved in the past when MGs were available only as powder or ribbons. To make use of unique properties, TFMGs with good GFA are evolving as alternative film materials which are potentially useful for many applications such as micro-electro-mechanical system (MEMS) devices. While MGs and BMGs are considered as newcomers, there are already many succinct and thorough articles reviewing various topics from the science of glass forming to atomic structure to mechanical properties [4–9]. However, only a short review on TFMGs published in 2010 [10] is available. The present review summarizes and discusses progress made in the area of TFMGs over the past decade. In addition, several challenging subjects will be proposed for future research.

2. Early work on TFMGs

Research on TFMGs in the 1980s and 90s mainly concern immiscible binary systems. These include Cu – Ta and Cu – W deposited by evaporation [11], as well as Cu – Zr [12] and Al – Fe, Bi – Fe and Bi – Ti [13]

by sputtering. Additional early studies on binary systems are those on the annealing-induced solid-state amorphization (SSA) of multilayer films [14–17]. In 1983, Schwarz and Johnson [14] fabricated the first La – Au TFMG by SSA during annealing of evaporated La/Au multilayer films. In 1986, Newcomb and Tu [16] and Cotts et al. [15] used transmission electron microscopy (TEM) and differential scanning calorimetry (DSC), respectively, to characterize the SSA of crystalline Ni/Zr multilayer thin films prepared by sputtering. Since then, some elemental multilayer films have been fabricated by evaporation and sputtering for SSA studies. See reference [18] for reviews and summaries of SSA.

Apart from binary systems and SSA multilayer films, which are often limited to nanometer-scaled thicknesses and narrow composition ranges, multi-component TFMGs readily become amorphous in the as-deposited state with film thicknesses up to several, or even tens of, micrometers. TFMGs gradually have received attention in scientific research for potential applications since the late 1990s because many new multi-component BMGs with good GFA in Mg-, Ln-, Zr-, Fe-, Pd-, Cu-, Ti-, and Ni-based systems have been developed by Inoue and his group in the 1980s and 90s [19]. Thin films prepared by vapor-to-solid deposition are expected to be farther from equilibrium than those prepared by a liquid-to-solid melting/casting process. Thus, the GFA can be further improved and composition ranges for amorphization are wider when formed by thin film processing such as sputtering [20,21]. In fact, sputter deposition technology has been used for GFA determination of metallic glass systems, by varying the film composition and density when co-sputtered with Zr and Cu elemental targets [22].

In 1999 and 2000, Zr – Cu – Al and Pd – Cu – Si ternary TFMGs were sputter deposited for MEMS applications [23,24]. Because of excellent three-dimension forming ability, good corrosion resistance, and mechanical properties, compared to conventional crystalline film counterparts, Zr- and Pd-based TFMGs are appropriate choices for MEMS applications, such as conical spring linear micro-actuators. Zr – Al – Cu – Ni TFMGs prepared by sputter deposition and focused ion beam patterning are reported for nano-device applications [25].

3. Unique properties

3.1. Annealing-induced amorphization of TFMGs

Amorphization in solids may be achieved by mechanical alloying, solid-state reaction or solid state amorphization (SSA), high pressure, or shock loading techniques. As mentioned in Section 2, in some elementally modulated crystalline films, SSA within the interfacial nanometer regions can occur through annealing-induced diffusion reactions [10]. Amorphization in sputtered TFMGs during annealing in the temperature range (the supercooled liquid region, SCLR or ΔT) between the glass transition temperature (T_g) and the crystallization temperature (T_x) has been reported. TFMGs which exhibit annealing-induced amorphization within ΔT include Zr- [26], Fe- [27], and Cu-based [28,29] systems. Yet, it is difficult to observe amorphization in TFMGs because the small scale of thin films and the presence of nanocrystalline phases have made characterization a challenging task. For instance, when Cu-based TFMG ($Cu_{51}Zr_{42}Al_4Ti_3$) with T_g and T_x determined to be 440.2 °C and 493.7 °C, respectively, is annealed within ΔT for various length of times [29], XRD spectra in Fig. 1 [29] from as-deposited and annealed films reveal samples are basically either amorphous or nanocrystalline, as indicated by typical broad diffraction humps with no detectable crystalline peaks. Based on the XRD results, annealing-induced amorphization can not be unambiguously determined because the films remain amorhpous or nanocrystalline with no obvious crystalline peaks up to 600 °C or after isothermal annealing at 470 °C for 3 min. Thus, the proper selection of analytical techniques to characterize the amorphous and crystalline structures is essential. In addition, it is important to carefully control the annealing process (such as the appropriate duration of annealing time under a protective atmosphere) for amorphization to take place.

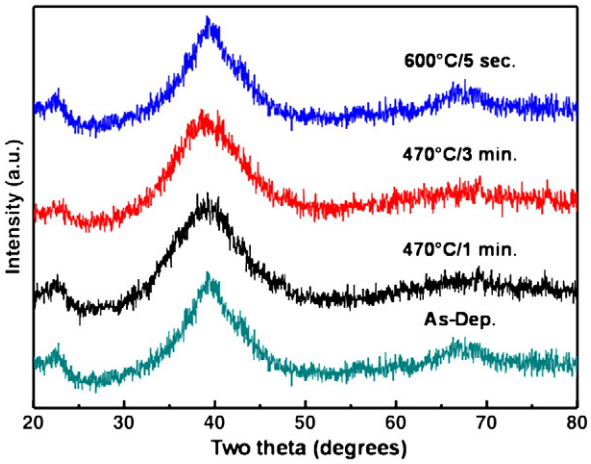

Fig. 1. XRD patterns from an as-deposited Cu-based TFMG and samples annealed within ΔT for various length of times [29].

The typical duration of time for annealing-induced amorphization in TFMGs is 1 min in ΔT. Transmission electron microscopy (TEM) is a common and useful tool for microstructural and crystallographic analyses.

As an example of amorphization within ΔT, Fig. 2 [27] shows TEM bright-field images and electron diffraction patterns of Fe-based TFMGs revealing that the minor nanocrystallites formed in the as-deposited state grow in size with annealing temperature up to 400 °C (T_g) and eventually transform into the amorphous phase within ΔT (*i.e.* at 500–550 °C). Above T_x, crystallization and grain growth of FeNi takes place at 600–750 °C. Amorphization also yields smooth film surfaces after annealing within ΔT, whereas the surface normally becomes rougher as the annealing temperature increases due to grain growth and crystallization. This can be clearly seen in the atomic force microscopy (AFM) topographic images in Fig. 3 that were acquired at the same temperatures as those in Fig. 2 for comparison [27]. The AFM images at 500 and 550 °C are featureless and consistent with those of the amorphous structure in TEM results (Fig. 2). In addition, the crystalline phases and their sizes in the film also affect surface morphology, *i.e.* the coarser crystalline grains at the higher temperatures in Fig. 2 have rougher surfaces in AFM results (Fig. 3).

To further clarify the above-described amorphization phenomenon, *in-situ* TEM observations are correlated with the *ex-situ* measurement results obtained using AFM and DSC. Figs. 4 and 5 show TEM bright-field images and corresponding diffraction patterns, respectively, of a Cu-based ($Cu_{51}Zr_{42}Al_4Ti_3$) TFMG heated to various temperatures [29]. Fig. 4(a) is an image obtained from the as-deposited sample, revealing small numbers of nanocrystallites in the amorphous matrix. Nevertheless, a columnar structure, typical of sputter deposition at low temperature [30], is revealed. The diffraction pattern in Fig. 5(a) indicates that the amorphous structure is the major phase with minor nanocrystallites. During heating at low temperatures [*e.g.* 400 °C, Fig. 4(b)], the spherical nanocrystallites increase in size, to 10–20 nm in diameter, and in number as well. The volume fraction of crystallites is estimated to be ~30%. The micrograph in Fig. 4(b) and its corresponding diffraction pattern in Fig. 5(b) indicate the nanocrystalline structures as minor phases within the dominant amorphous matrix. The nanocrystallites produce a spotty diffraction pattern, which has been identified as either tetragonal or cubic $Cu_{10}Zr_7$. At this temperature (400 °C), the large interfacial energy drives coarsening of the metastable crystalline phase through a process analogous to Ostwald ripening and the nanocrystallites thus increase in size. Fig. 4(c) shows a fully amorphous structure with no observable crystalline phase in the TEM image after heating at 438 °C within the ΔT range. The typical broad diffuse diffraction ring further confirms the amorphous nature of Fig. 5(c). Neither obvious crystals nor splitting of the halo ring is observed in the bright-field TEM image or

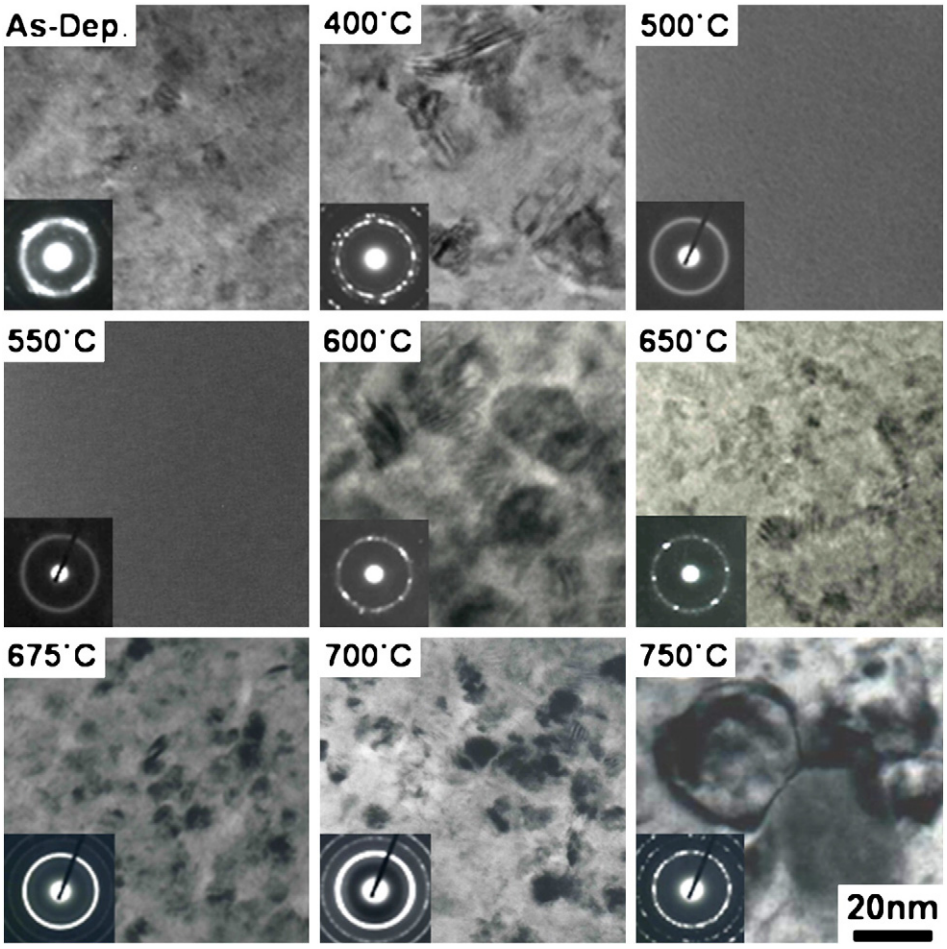

Fig. 2. TEM bright-field images and diffraction patterns from Fe-based TFMGs revealing phase evolution during one-min anneals: amorphous matrix with γ-fcc FeNi nanocrystallites (as-deposited) → growth of nanocrystallites (up to 400 °C) → amorphous (500 °C and 550 °C) → formation of cubic Fe(Ni) crystallites (600 °C) with minor cubic FeNi phase (650 °C to 700 °C) → formation and grain growth of FeNi phase (750 °C) [27].

diffraction pattern. At this point, the metastable nanocrystalline phases may have dissolved in the amorphous matrix. As the temperature rises to 525 °C, well above the crystallization transition temperature, nanocrystallites reappear in the amorphous matrix [Fig. 4(d)]. Appearance of crystalline spots in the diffraction pattern of Fig. 5(d) indicates that the amorphous phase starts to transform into the crystal state as the temperature increases. The sizes of nanocrystalline phases at 525 °C are in the range of 20 to 35 nm.

3.2. Smooth surface

In BMGs, surface defects on the scale of a few micrometers tend to disappear without crystallization as the glassy surface undergoes "self-healing" when heated within ΔT due to a sufficiently low viscosity [31]. In the case of TFMGs, both amorphization and low viscosity are thought to cause the recovery of minor scratches, such as a nanoindentation mark. AFM images in Fig. 6 reveal a decrease in the size of a nanoindentation after annealing within ΔT. The indentation, measured using AFM, becomes ~13.8% shallower in depth, decreasing from 64.63 ± 0.82 nm to 55.97 ± 0.53 nm, after annealing in ΔT for 1 min. The figure shows that the film surface is also smoother and the pile-up around the indentation decreases as a result of annealing. According to AFM and TEM results, annealing-induced amorphization within ΔT provides a unique and advantageous property for TFMGs over other types of thin films because smooth surfaces can be readily obtained through a proper annealing process.

3.3. Hardness and electrical resistivity

Annealing-induced amorphization is generally associated with significant alterations in film properties. These property changes, in addition to the smooth surface shown in Fig. 3, include a decrease in hardness and an increase in electrical resistivity [26–28]. The hardness drop (or softening) within ΔT is mainly due to the single phase of amorphous structures, compared to composite structures consisting of crystalline phases in the amorphous matrix annealed at temperatures other than ΔT [27,28]. Overall, the film hardness tends to increase with the temperature upon annealing up to T_g, as reported for several TFMG systems [26,27,29,32]. The hardness increases are thought to be attributable to the combined effects of composite structure and free volume annihilation due to structure relaxation.

For electrical property changes due to amorphization within ΔT, Fig. 7 shows an example of the dramatic increase in the electrical resistivity of Cu-based ($Cu_{51}Zr_{42}Al_4Ti_3$) TFMGs [28]. According to differential scanning calorimetric (DSC) scan data in Fig. 7(a), T_g, T_x, and ΔT are determined to be 452 °C, 502 °C, and 50 °C, respectively. In Fig. 7(b), annealing within the ΔT region is shown to cause a distinct increase in the film resistivity to a maximum of ~4628 μΩ-cm at 502 °C. When the temperature reaches 527 °C, the resistivity then decreases to ~177 μΩ-cm. The random atomic structure in the amorphous phase is believed to cause the electrical resistivity increase within ΔT, while the presence of crystalline phases in the films annealed at temperatures other than ΔT result in relatively low resistivity. The extent of resistivity change within ΔT is larger in Cu-based TFMGs than those reported for Zr- and Fe-based TFMGs [26,27]. The

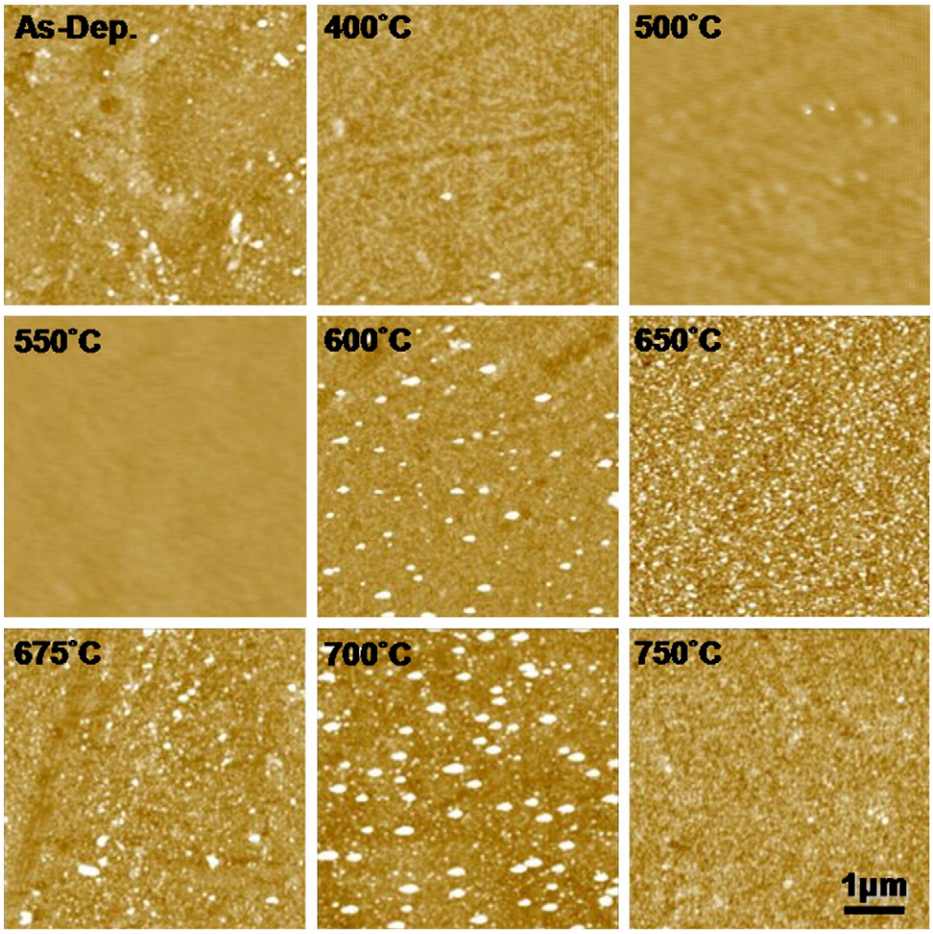

Fig. 3. AFM topographic images ($5 \times 5\ \mu m^2$, height scale = 50 nm) of Fe-based TFMGs in as-deposited and annealed (one min) conditions.

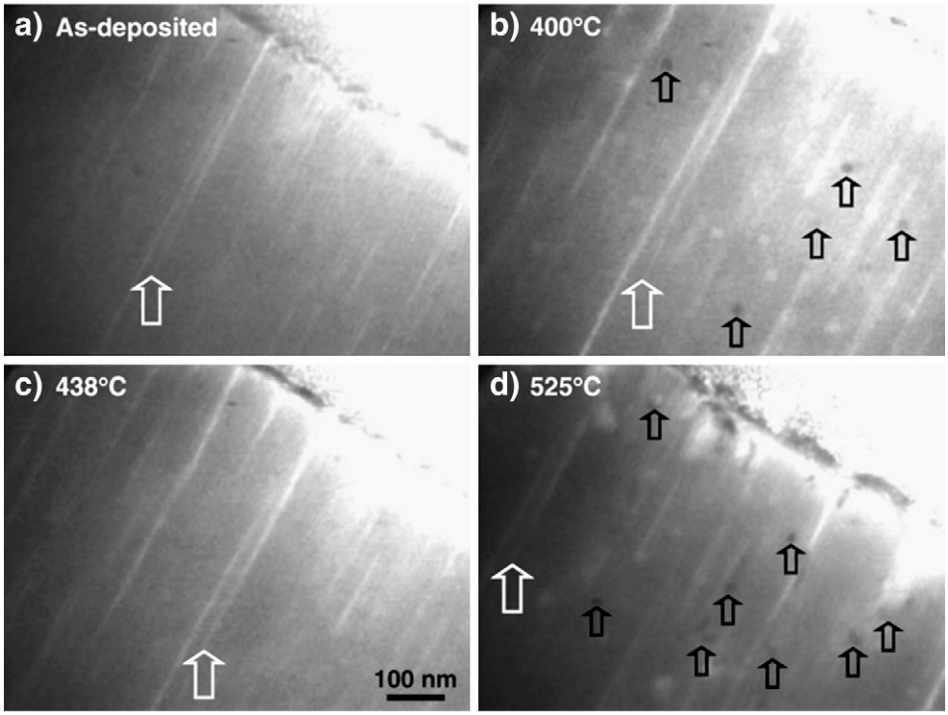

Fig. 4. *In-situ* TEM video image frames of a Cu-based TFMG: (a) as-deposited and after one-min anneals at (b) 400 °C, (c) 438 °C and (d) 525 °C. Approximately same locations in the images are denoted by white reference arrows. Black arrows indicate the presence of crystalline phases [29].

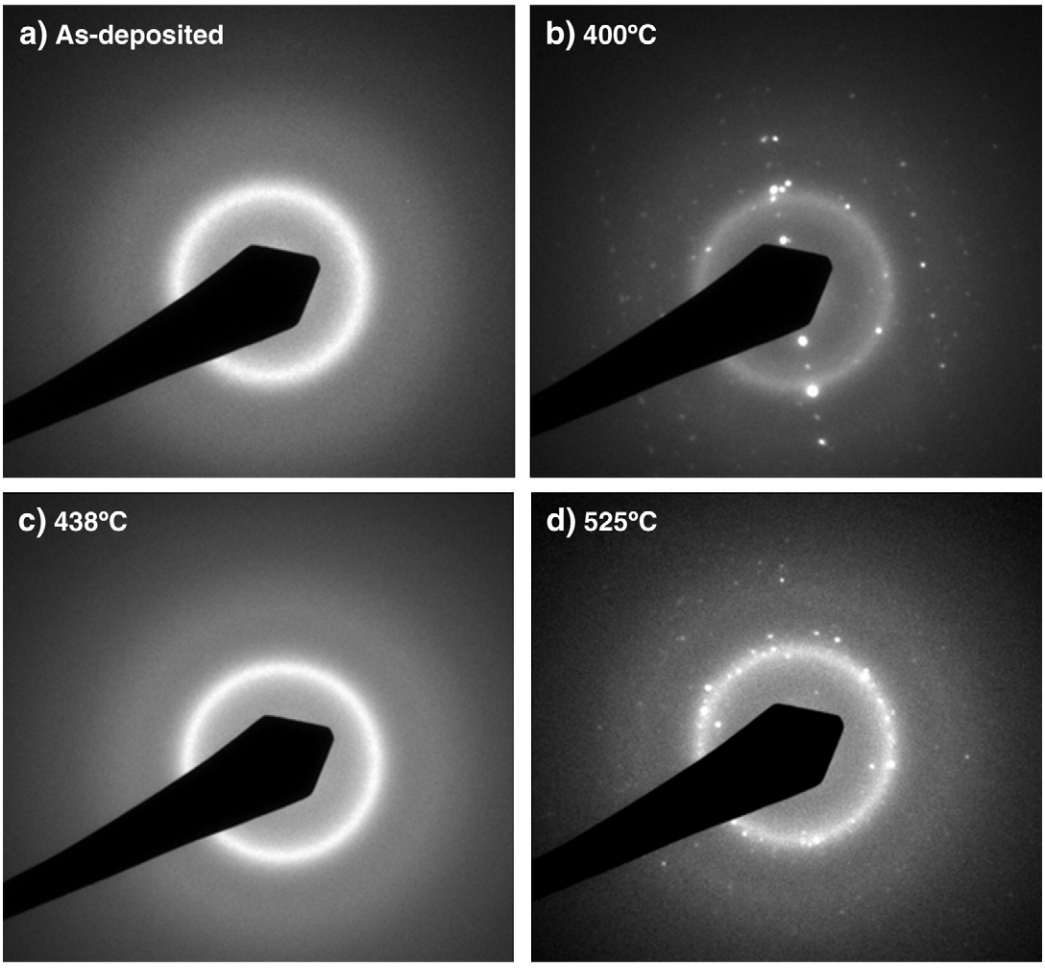

Fig. 5. *In-situ* TEM diffraction patterns of a Cu-based TFMG: (a) as-deposited and after one-min anneals at (b) 400 °C, (c) 438 °C and (d) 525 °C. Major diffraction spots in (b) are indexed to be the $Cu_{10}Zr_7$ phase, while those in (d) are from $Cu_{10}Zr_7$ and $AlZr_2$ [29].

significant increase (~25×) of resistivity in this case may have a potential for applications such as safety breakers and switches where rapid electrical resistivity change with temperature is required.

3.4. Magnetic properties

Thermal annealing affects not only microstructural, surface morphology, hardness, and resistivity, but also the magnetic properties of Fe-based TFMGs [27]. Magnetic force microscopy (MFM) images in Fig. 8 show variations in the magnetic domain structure upon annealing. Until the temperature reaches 600 °C, there is no obvious color contrast in the images, suggesting the magnetization direction lies in the plane of the film. Since the film thickness in this case is about 500 nm, which is relatively thin, the demagnetization energy in the film is negligible due to the high aspect ratio of film geometry and thus a single domain structure is formed. Furthermore, the domain structure formation is not affected by amorphization at 500 and 550 °C.

When the temperature reaches 650–700 °C, the color-contrast MFM images show the distinctive features of a “dark” and “bright” stripe magnetic domain structure. Since the MFM tip is magnetized downward, the bright stripe domains are those with magnetization upward, whereas the dark domains are magnetized downward. The “dark/bright” stripe images indicate the presence of strong perpendicular magnetic anisotropy with the magnetic easy axis normal to the plane of the film. As the magnetization is along the easy axis and normal to the film plane, the film demagnetizing fields in the film increase. To

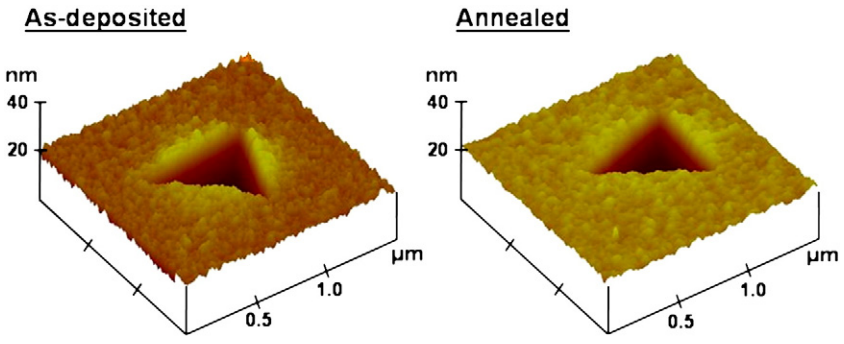

Fig. 6. AFM images showing the recovery of a nanoindentation in a Zr-based TFMG after annealing at 460 °C for 1 min.

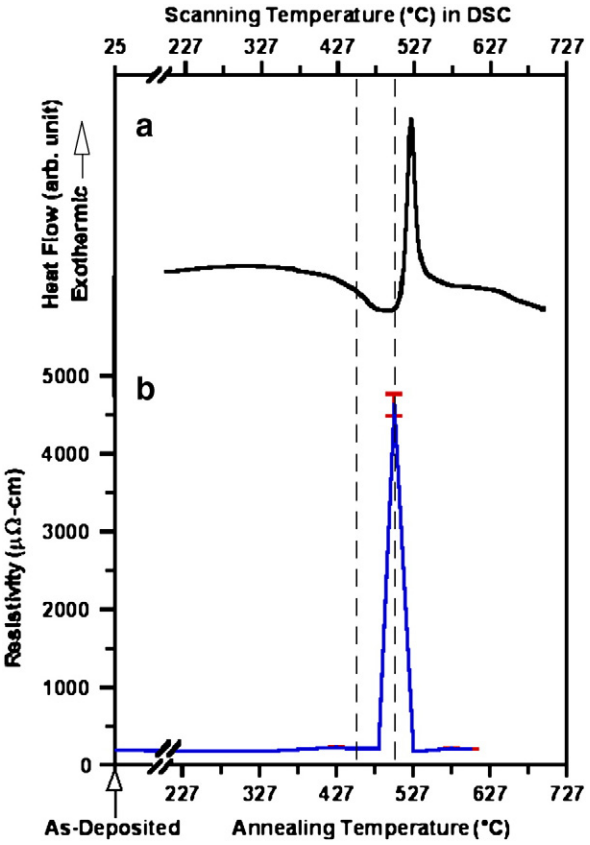

Fig. 7. (a) DSC and (b) electrical resistivity results for Cu-based TFMGs in as-deposited and annealed (for one min) conditions. Dashes lines indicate approximate ΔT window [28].

minimize the demagnetizing fields, the bright and dark stripe domain structures are thus formed. The stripe domains are found to increase in width with annealing temperature between 650 and 700 °C, which increases the effective magnetic anisotropy field in the film [27]. The annealing-induced perpendicular magnetic anisotropy originates from the positive magnetostriction and the compressive stress due to the large FeNi lattice phase present in the smaller Fe(Ni) lattice matrix [27]. When the film is annealed at 750 °C, the magnetic anisotropy vanishes because the stress diminishes due to the absence of minor phases, resulting in no apparent color contrast in the magnetic force image. This "stress-induced perpendicular magnetic anisotropy" is commonly reported in multilayered films, but is rare in single layer thin films [33,34]. This again exemplifies TFMGs as fascinating thin film materials exhibiting unique and extraordinary properties, many of which have not been explored or well studied.

3.5. Glass-forming ability (GFA)

For TFMG deposition, amorphous sputtering targets are difficult to prepare because of the large sizes. However, a recent work by Chen et al. reported that both amorphous and crystalline targets yield no apparent differences in film microstructure and crystal structure [35]. In addition, it is well known that the composition window for achieving amorphous thin films is much wider than that for achieving BMGs by rapid casting because the state produced by the vapor-to-solid deposition is farther from equilibrium than the state produced by the liquid-to-solid casting process. For instance, fully amorphous thin films can be easily prepared by co-sputtering of Zr–Cu or Zr–Cu–Ti systems [20,21]. Partially amorphous thin films are achieved by co-sputtering of Mg–Cu based alloys [36]. Some elements having positive heat of mixing with the parent element can still be retained in the amorphous matrix of TFMG prepared by sputtering. As an example, Zr-based TFMGs with immiscible Ta are successfully fabricated via co-sputtering [21,37]. The Ta content in Zr-based TFMGs ranges from 0 to ~75 atomic percent (at.%); thus, the GFA is distinctly larger than those of BMGs. When the Ta content is over 75 at.%, the amorphous TFMG structure gradually transforms to include nanocrystalline β-Ta, as shown in the TEM results in Fig. 9 [20,36]. The mechanical properties are strongly influenced by the Ta content. The film's elastic modulus remains nearly constant with 0–50 at% Ta, but increases rapidly at 50–100% Ta. The key factor appears to be the population of strong Ta–Ta bonds. The highest elastic modulus and hardness, ~140 GPa and 10 GPa, respectively, of Ta-rich TFMGs, much higher than for Zr-, Cu and Ti-based amorphous counterparts, might be useful for applications in the area of hard coatings or interlayers for diffusion barriers.

3.6. Mechanical properties

3.6.1. Residual stress

Residual stress, either in compression or tension, in magnetron sputtered films is associated with the film/substrate lattice misfit, energetic-particle bombardment, and deposition conditions such as working pressure and substrate bias. The presence of residual stress plays a vital role in altering mechanical properties of film and substrate, including film hardness, adhesion, and substrate fatigue. In a previous study on a Zr-based TFMG ($Zr_{47}Cu_{31}Al_{13}Ni_9$) [38], a 200 nm-thick film is reported to exhibit a compressive residual stress of 88.2 MPa on a Si(001) wafer, as determined by substrate curvature measurements. According to Stoney's equation,

$$\sigma_f = \left\{\frac{M_s}{6(1-\nu_s)}\right\}\left(\frac{t_s^{\,2}}{t_f}\right)\left(\frac{1}{R}-\frac{1}{R_0}\right), \quad (1)$$

where σ_f is the residual stress in the film, t_f the film thickness, t_s the substrate thickness, M_s the biaxial modulus of the substrate (180.3 GPa), and ν_s is the Poisson's ratio of the substrate. R_0 and R are the radii of curvature of the substrate before and after the film deposition, respectively. Small compressive stress in thin films is generally favorable for increasing the resistance to crack initiation and inhibition of crack propagation [38]. Improvement of fatigue-properties on steel substrates due to the presence of Zr-based TFMGs will be discussed in a subsequent section of this article.

It is important to further evaluate the influence of deposition conditions (such as substrate bias) on the film residual stress. The compressive stress in Zr-based TFMGs increases from 88.2 MPa without bias to 764.3 MPa with 125 V bias, an increase of ~8.6×. The residual stress drops noticeably to 441.7 MPa, a ~42% decrease, when an ~10-nm-thick Ti buffer layer is deposited between the bias-grown film and the Si substrate.

The results in Fig. 10 show the compressive stresses present in Zr-based TFMGs and the increasing trend of stress with film thickness when a −125 V bias is applied to the Si substrate during deposition. Bias-deposited Zr-based TFMGs have a compressive stress of 7.8 GPa, when the film thickness is 800 nm.

The effect of bias on the film microstructure is also pronounced, as shown in the TEM micrographs of Fig. 11. It is seen that the film in this case becomes much denser, the column size decreases to ~11 nm, and nanocrystallites are not apparent, as compared with that deposited without bias in Fig. 4. The significant increase in the residual stress and film density is attributed to the ion bombardments when the bias is applied.

3.6.2. Nanoindentation

To characterize the mechanical properties of TFMGs, nanoindentation is a convenient approach since the film hardness and Young's

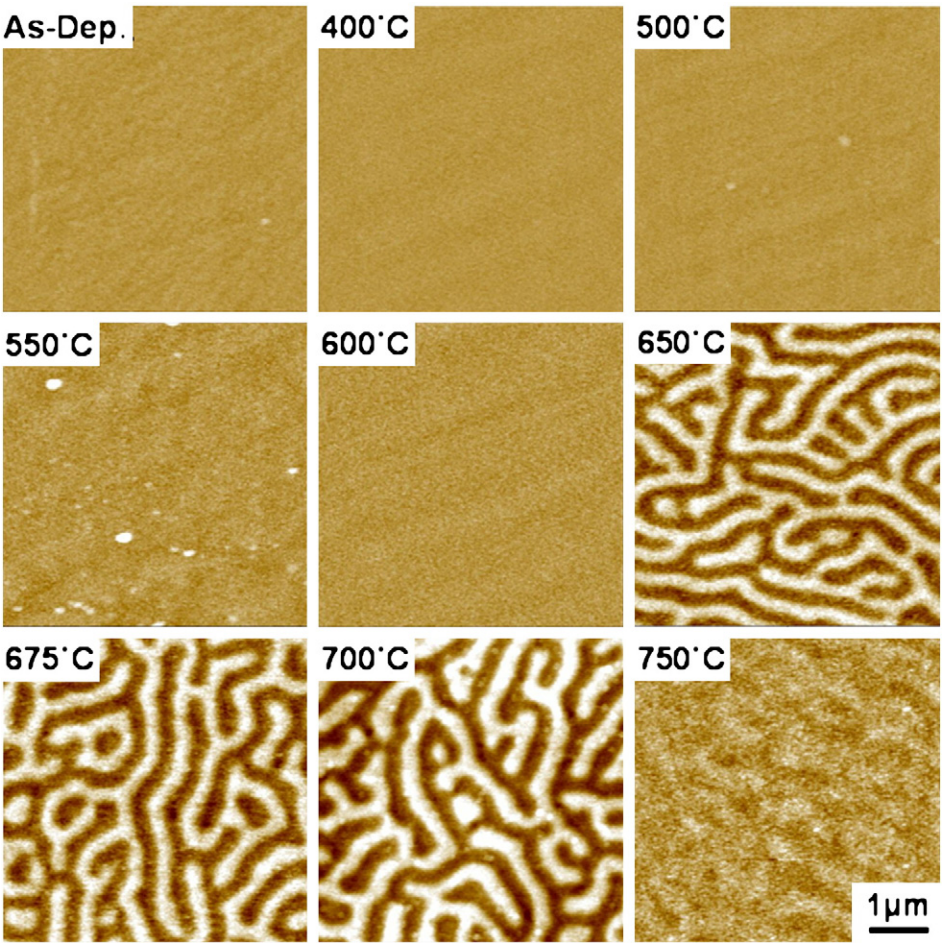

Fig. 8. MFM images ($5\times5\ \mu m^2$) of Fe-based TFMGs as-deposited and annealed for 1 min at several temperatures [27].

modulus can be obtained experimentally [10,39,40]. However, as with other film materials, care should be taken when interpreting the experimental results derived directly from indentation load-displacement curves using the well established Oliver and Pharr (OP) method for bulk materials [41]. In principle, when the OP method is utilized in data processing for a TFMG, the indentation hardness and modulus obtained reflect not only the mechanical attributes of the film, but also those of the underlying substrate. To circumvent this difficulty, a sequential-nanoindentation approach can be employed to obtain the 'intrinsic' properties of the film through data fitting. Fig. 12(a) displays a typical load-time curve consisting of multiple loading and unloading cycles for sequential nanoindentation. As an analog of a conventional nanoindentation test, each cycle is composed of loading, holding, and unloading segments, from which the hardness and Young's modulus data can be derived using the OP method as a function of the indentation depth as shown in Fig. 12(b).

As a demonstration, Zr-based ($Zr_{53}Cu_{29}Al_{12}Ni_6$) TFMGs with thicknesses of 200, 400, 600, 800, and 1000 nm on Si(001) substrates were used for the nanoindentation evaluation. Nanoindentation tests were carried out with resolutions of 0.1 μN in load and 1 nm in displacement. Young's modulus and hardness of a bare Si substrate were first determined to be 187 ± 8 GPa and 12.5 ± 0.4 GPa, respectively, in the range of indent depths from 300 to 1500 nm. These values are consistent with those reported for Si(001) [42]. Sequential nanoindentation measurements were then performed on films with different thicknesses. Young's modulus and hardness values display strong indentation-depth dependence, particularly for normalized contact depth h/t_f exceeding ~10%, as shown in Fig. 13(a) and (b), where h and t_f denote indentation-depth and film thickness, respectively.

To extract Young's modulus of the film, a modified King's model is used [43]:

$$\frac{1}{E_r}=\frac{1-\nu_i^2}{E_i}+\frac{1-\nu_f^2}{E_f}\left(1-e^{-\frac{\gamma\left(t_f-h\right)}{a}}\right)+\frac{1-\nu_S^2}{E_S}e^{-\frac{\gamma\left(t_f-h\right)}{a}}, \tag{2}$$

where E_r is the reduced 'composite' modulus of the film/substrate system obtained via the original OP method [41]. E_i, E_f, E_s and ν_i, ν_f, ν_s denote the Young's modulus and the Poisson's ratio of the diamond indenter, film, and Si(001) substrate, respectively, a the effective contact radius approximated as $a\approx2.8\,h$ for the Berkovich nanoindenter, and γ is a weighting factor that accounts for the continuously changing contribution of the film and substrate to the overall stiffness [43]. According to this equation, it can be readily seen that the reduced modulus of the film/substrate system is dominated by the properties of the film only when h/t_f approaches zero. Also from this equation, the trend of the reduced composite modulus vs. h/t_f can be fit as shown in Fig. 13(a). Here, the values of E_i and ν_i are taken to be 1140 GPa and 0.07, respectively, for the diamond indenter, while ν_f and ν_s are assumed as 0.36 and 0.28 for Zr-based TFMG and the Si substrate [44,45]. To fit the experimental data, E_f, E_s and γ are treated as fitting parameters. Through nonlinear data fitting, the values of the three fitting parameters were obtained, as tabulated in Table 1.

Similar to the trend for the reduced composite modulus, the hardness of the films also levels off as h/t_f approaches zero, implying a diminishing substrate effect when the indent depth decreases. According to the result in Fig. 13(b), the depth-insensitive hardness for the current film/substrate system corresponds to h/t_f~0.1. However, it is worth

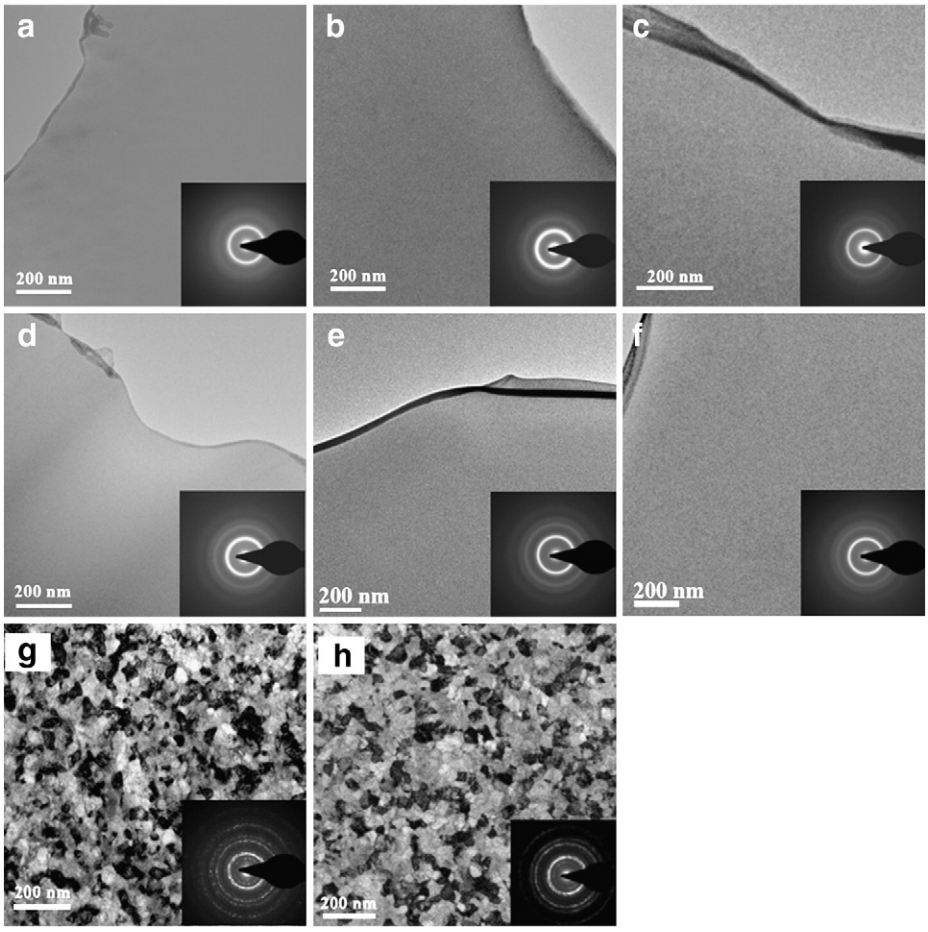

Fig. 9. Bright-field TEM images of Zr-based TFMGs with various Ta contents: (a) $Zr_{45}Cu_{27}Ti_{15}Ta_{13}$, (b) $Zr_{41}Cu_{23}Ti_{12}Ta_{24}$, (c) $Zr_{31}Cu_{15}Ti_{10}Ta_{44}$ (d) $Zr_{10}Cu_5Ti_3Ta_{57}$ (e) $Zr_{19}Cu_6Ti_7Ta_{68}$, (f) $Zr_{14}Cu_7Ti_5Ta_{74}$, (g) $Zr_{10}Cu_5Ti_3Ta_{82}$, and (h) $Zr_4Cu_3Ti_1Ta_{92}$. Selected area diffraction patterns are shown in insets [21].

noting that there is a limit for continuously reducing the indent depth in a nanoindentation test, below which uncertainties arise, due to imperfections in the nanoindenter tip. For this example, the minimum indent depth is approximately 30 nm, which is ~15% of the 200 nm film thickness. As a consequence, the hardness of the 200-nm film seems not yet saturated and still remains above the value devoid of the substrate effect [Fig. 13(b)]. For the sake of comparison, the apparent hardnesses of the films obtained at h/t_f~0.15, which is closest to the true film property, are listed in Table 1.

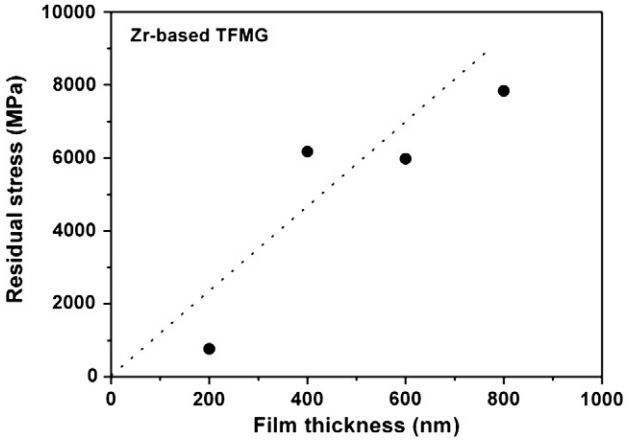

Fig. 10. Relationship between the residual compressive stress and film thickness of Zr-based TFMGs sputter deposited with a −125 V bias on Si(001).

From the tabulated results, a thickness effect on the film modulus is observed. As the thickness decreases from 1000 nm to 200 nm, the corresponding modulus increases by nearly 20%, from 107 GPa to 128 GPa. However, considering the 10% data scattering in the modulus measurement [the error bar in Fig. 13(a)], such an increase in the Young's modulus may not be significant. However, at a relatively large h/t_f, there is a tendency to overestimate the Young's modulus of the TFMG due to the indentation pile-up effect [46]. Thus, the fitted E_f values may be systematically biased if the majority of the data points used for data fitting are affected by indentation pile-up, which could result in a fitted E_f higher than its actual value, particularly for the relatively thin TFMGs, as shown in the AFM analyses of nanoindentations in Fig. 14. In this figure, the

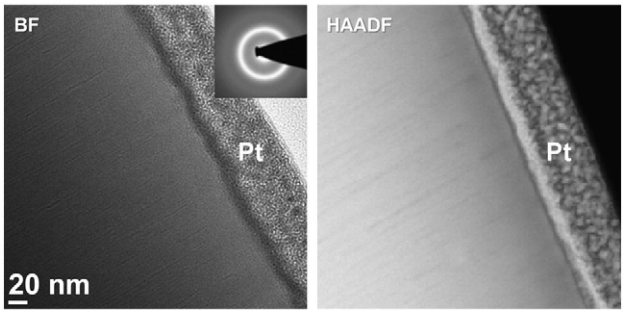

Fig. 11. Cross-sectional TEM bright-field (BF) image, with a selected-are diffraction pattern in the inset, and a Z-contrast high-angle annular dark-field (HAADF) micrograph of a Zr-based TFMG sputter deposited with a −125 V bias on Si(001). The Pt cap is deposited as a protective layer for FIB sample preparation.

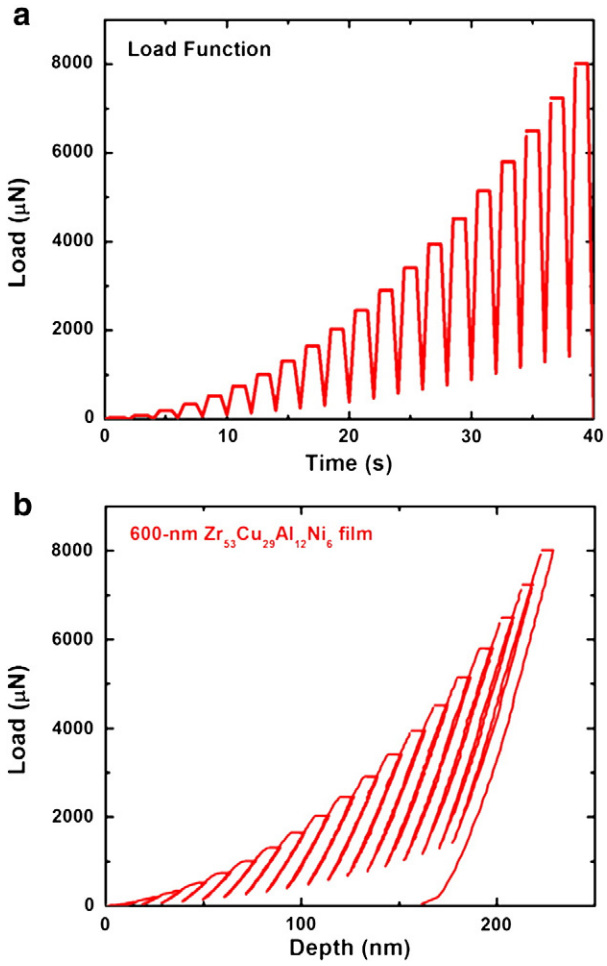

Fig. 12. Typical sequential nanoindentation results from a 600-nm-thick Zr-based TFMG on Si(001) substrate: (a) load-time and (b) load-displacement (depth) curves.

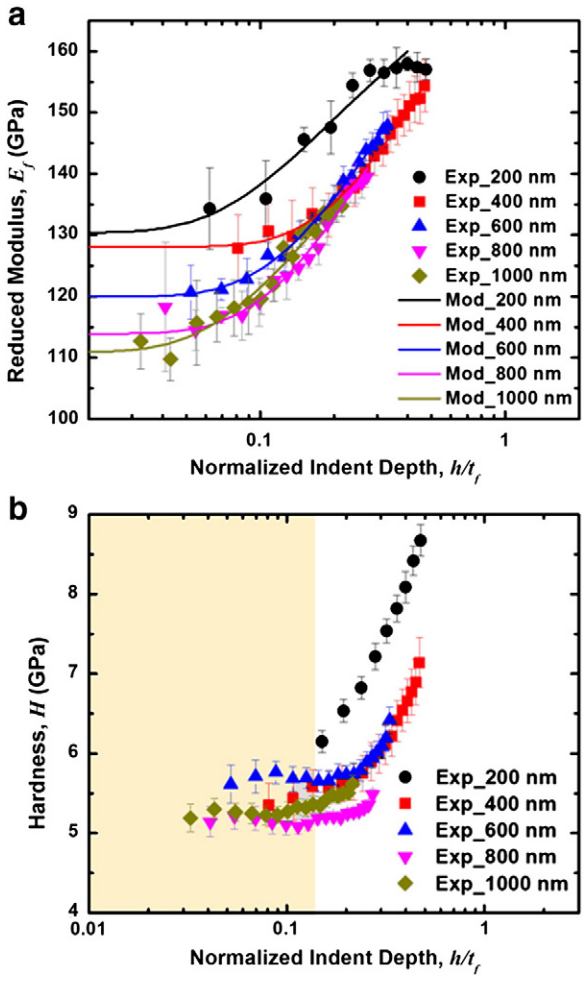

Fig. 13. Variations of the (a) reduced modulus and (b) hardness as a function of the normalized contact depth h/t_f for Zr-based TFMGs on Si(001) substrates. The error bars correspond to the standard deviation of the experimental data obtained at different indentation sites. The solid curves in (a) are plotted based on a modified King's model [43]. The shaded area in (b) indicates the range in h/t_f where the indentation hardness becomes insensitive to the indent depth.

pile-up is more apparent when the film thickness decreases. Considering all these facts, the modulus of the MG films is taken as the average of all fitted results, which is 117 ± 9 GPa, in order to avoid over-estimation. This gives a Si substrate modulus of 183 ± 8 GPa, which is in excellent agreement with the result obtained from nanoindentation of the bare Si substrate.

Compared to the film modulus, the film hardness measured at h/t_f ~ 0.15 oscillates around ~5.5 GPa, displaying no clear sign of a thickness effect except for the 200-nm film exhibiting a hardness of ~6.5 GPa, ~20% higher. While the hardness does not appear to increase with film thickness, other thickness effects may be playing in role. These include residual stress and underlying substrate and indentation pile-up [47].

3.6.3. Microcompression

In the MG literature, microcompression measurements on micropillars, fabricated using the focused ion beam (FIB) technique, have been used to study the size effect on shear-banding mediated plasticity [48–52]. This is because the macroscopic deformability of MG at room temperature is a shear-band dominated phenomenon and shear band formation becomes important to study at the small scale. The emphasis here is placed on the application of microcompression methodology, emphasizing its functionality as a tool for mechanical characterization of TFMGs. Unlike nanoindentation, microcompression enables nearly uniaxial-loading on micropillars, which makes it attractive as an analog of the conventional compression test, thus facilitating the interpretation of experimental findings. However, issues like the geometrical imperfection of the FIB-milled micropillars (pillar tapering) [46], the substrate compliance [46], and FIB-induced surface radiation damage [48], complicate the translation of experimental data into the intrinsic material properties; this can lead to serious concern as to whether the mechanical properties obtained from microcompression are comparable with those obtained from bulk testing [53]. For TFMGs, further difficulty stems from the underlying supporting substrate, which could result in a biased estimation of the film mechanical properties if not accounted for appropriately. Despite these pitfalls, microcompression methodology has been widely utilized for mechanical testing of a variety of materials [54].

Similar to nanoindentation, control experiments must first be performed for characterizing the mechanical properties of the Si(001) substrate. To this end, micropillars are fabricated on the surface of the wafer

Table 1
Physical properties extracted from sequential nanoindentation analyses of $Zr_{53}Cu_{29}Al_{12}Ni_6$ TFMGs with different thicknesses (t_f). E_s is Young's modulus of the Si(001) substrate and E_f is Young's modulus of the film. Note that the hardness H corresponds to that at normalized contact depth h/t_f ~ 0.15 where h is the contact depth.

t_f (nm)	E_s (GPa)	E_f (GPa)	H (GPa)
200	184	128	6.5 ± 0.1
400	191	125	5.6 ± 0.2
600	189	117	5.7 ± 0.2
800	178	110	5.2 ± 0.1
1000	172	107	5.4 ± 0.1

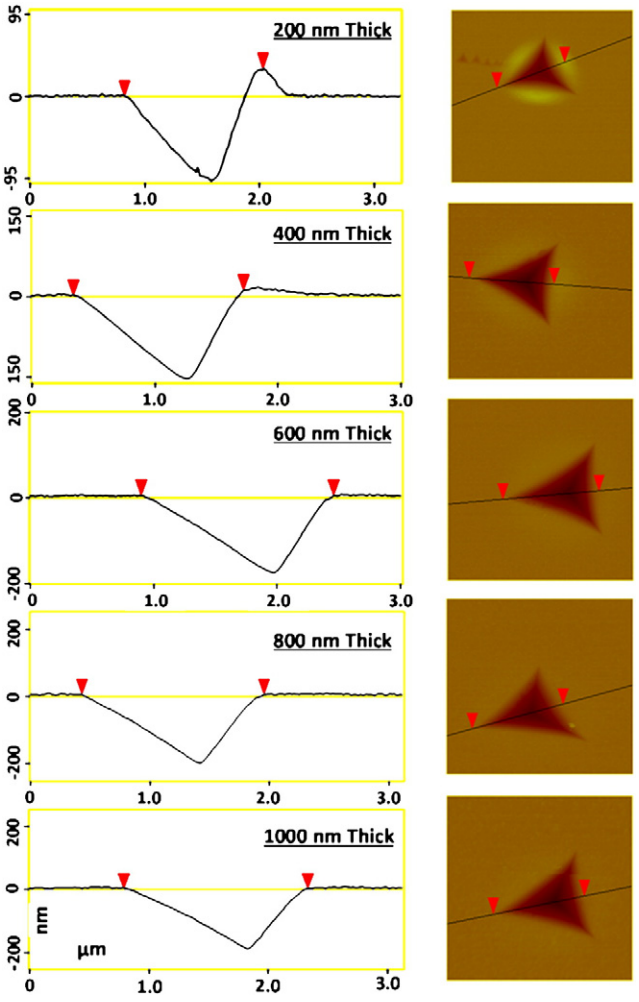

Fig. 14. Section analyses (left) and AFM height images (right) of nanoindentations in $Zr_{53}Cu_{29}Al_{12}Ni_6$ TFMGs of various thicknesses, showing the thickness effect on indentation pile-up. All the indents were made at the same peak load of 8 mN.

using FIB. In the microcompression literature, there are two approaches to FIB machining, *i.e.*, the ion-beam lathe [55,56] and the sequential ion-beam milling approach [57]. The former approach enables the machining of materials to form non-tapered cylindrical pillar shapes, but it is time consuming and limited to micro-sized pillars. In contrast, the latter approach is time efficient for obtaining pillars at the submicron size, but generally results in a tapered pillar shape [46,54]. Thus, it is generally a compromise decision to select the appropriate approach which fits a particular research object. Here, the sequential ion-beam milling method is adopted to prepare micropillars for microcompression of TFMGs. The details of FIB milling have been thoroughly described elsewhere [46,57].

Fig. 15(a) shows the typical shape of a tapered micropillar milled into an uncoated Si(001) wafer. By replacing the Berkovich nanoindenter with a flat-end diamond nanoindenter, 20 μm in diameter, the same nanoindentation system can be modified for microcompression under either load or displacement control. After microcompression, the deformed or fractured micropillars are examined by electron microscopy. As shown in Fig. 15(b), a Si micropillar with a diameter of 1 μm and an aspect ratio of ~2 shattered into many pieces after microcompression, a signature of the intrinsic brittleness of Si, even at the micro-scale. Likewise, micropillars coated with TFMGs can be fabricated using FIB, as shown in Fig. 15(c) to (f) for $Zr_{53}Cu_{29}Al_{12}Ni_6$ TFMGs. In this way, one can vary the shape and size of the micropillars for a systematic investigation of the substrate effect, which is analogous to changing the indent depth in nanoindentation.

Fig. 16(a) displays typical load-displacement curves obtained from a set of micropillars with dimensions 1 μm × 3 μm. The experimental results include uncoated Si and Si coated with $Zr_{53}Cu_{29}Al_{12}Ni_6$ TFMGs, from which it can be seen that the uncoated Si micropillars fractured at much higher loads than those causing yielding in the TFMGs. Since the uncoated Si micropillars behave elastically before fracture, the mechanical response of the TFMGs can therefore be extracted by subtracting the displacement of the Si underlayer from the total displacement measured, as shown in Fig. 16(b). For a monolithic Si micropillar, the load-displacement response in microcompression can be expressed as: [46]

$$P = E_{Si} f\left(\frac{H}{D}, \beta, \nu, \frac{\rho}{D}\right)\frac{\pi D^2}{H}\delta_{Si}, \tag{3}$$

where P is the applied load; E_{Si}, H, D, β, ρ and ν denote the Young's modulus, height, diameter, taper angle, radius of curvature at the base, and Poisson's ratio of the Si micropillar, respectively, as shown in Fig. 16(b); δ_{Si} is the displacement of the Si micropillar. Here, f is the dimensionless function defined in Reference [46]. Because of the complexity of this function, for the sake of brevity, readers are suggested to refer to the original paper [46] for further details.

The displacement δ_f occurring in the TFMG is $(\delta - \delta_{Si})$, where δ is the total displacement measured during microcompression. It should be noted that E_{Si} differs from that measured from nanoindentation owing to the elastic anisotropy of Si. E_{Si} can be extracted directly from microcompression of uncoated Si micropillars. Due to the uniaxial stress field applied for microcompression, E_{Si} should be close to the out-of-plane modulus along the <100> direction, while the indentation modulus reflects a value averaged over those sampled by the complex indentation stress field. Based on experimental microcompression data , E_{Si} is found to be ~130 GPa, which is consistent with the theoretical value [45]. Once E_{Si} is known, the TFMG load-displacement curves can be extracted, as shown in Fig. 16(c). From these curves, the film's Young's modulus and apparent yielding strength can be estimated by assuming a uniform film cross section and using the data from films on micropillars with a taper angle less than 2°. In doing so, the Young's modulus of the TFMGs was found to be 108 ± 15 GPa, irrespective of film thickness. This is very close to the nanoindentation results.

Unlike the Young's moduli of TFMGs, their apparent yielding strengths exhibit strong shape dependence, as shown in Fig. 17. Regardless of the film thickness, the apparent yield strengths remain approximately constant at ~2.6 GPa for a film thickness to pillar diameter ratio, t_f/D, greater than ~0.5, while they increase dramatically for $t_f/D < 0.5$. This phenomenon of shape dependence has a simple physical explanation. According to Packard et al. [58], global yielding occurs in MGs when material on a potential shear plane reaches the yielding point. For TFMGs with a high aspect ratio t_f/D, the stress state is closer to uniaxial and it is easy to form a potential shear plane without the hindrance of the underlying substrate. However, for TFMGs with a low aspect ratio, the stress state is closer to triaxial, particularly in regions near the film/substrate interface. In this case, global yielding does not occur until the applied stress is increased to a higher level to cause local yielding of material at the interface where a strong compressive stress exists. That is to say, the substrate effect arises once a potential shear plane is impeded by the film/substrate interface. Assuming a 45° shear angle, one can then estimate the critical aspect ratio t_f/D triggering such a shape effect to be approximately ~0.5, at which point the shear plane from the film center just intersects the interface (see the insets in Fig. 17). Based on these experimental findings, it is concluded that the compressive yield strength of $Zr_{53}Cu_{29}Al_{12}Ni_6$ TFMGs, with minimized substrate effects and therefore comparable with that of their bulk counterparts, should be ~2.6 GPa.

It is worthwhile to point out that, even though BMGs are quite brittle under uniaxial loading without noticeable plasticity at room temperature, TFMGs appear very ductile as can be seen from load-

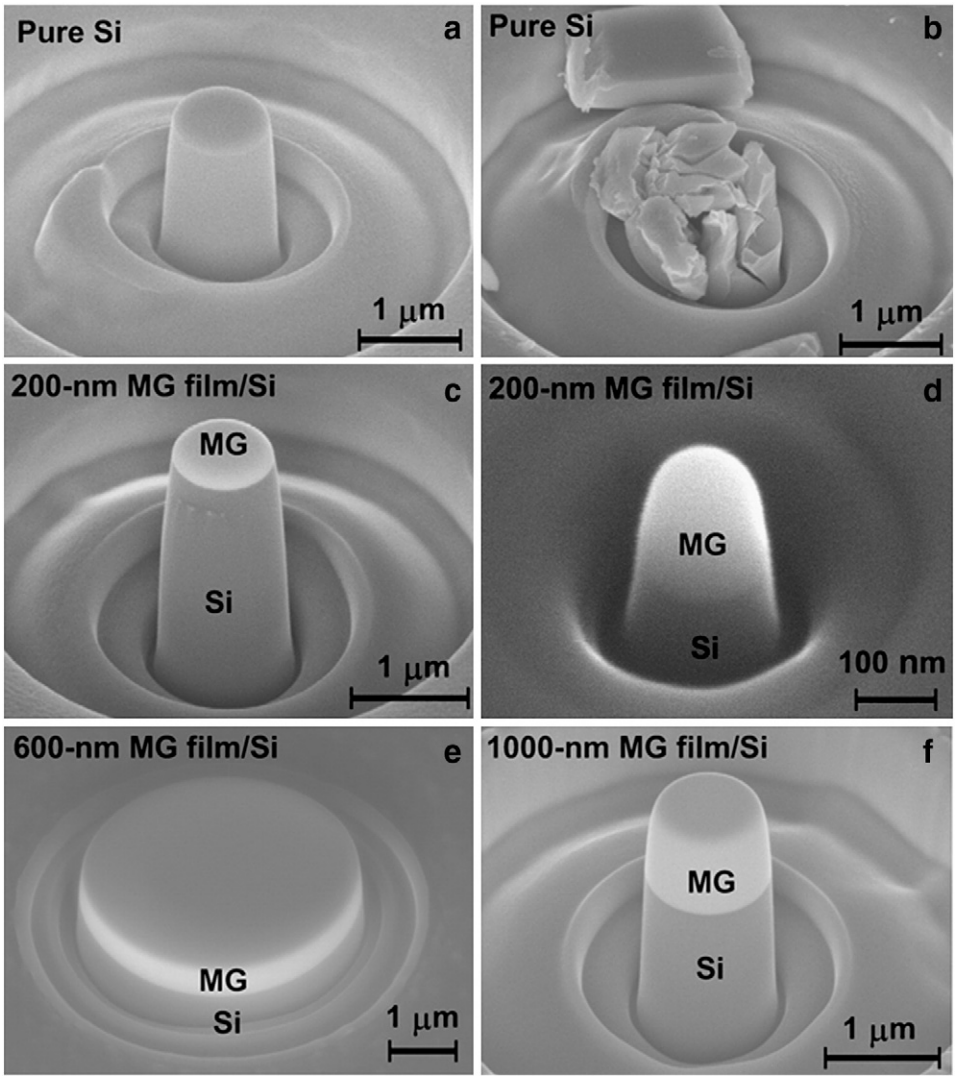

Fig. 15. SEM micrographs of (a) as-fabricated and (b) fractured Si micropillars on an uncoated Si(100) substrate; (c) to (f) as-fabricated micropillars, different sizes and shapes, coated with Zr-based TFMGs.

displacement curves in Fig. 16(c). In general, this size-effect behavior can be attributed to stable shear banding in MGs at a small size scale (typically less than 1 mm), which is then related to a size-affected elastic energy release upon yielding [48,49,51,52,59–61]. However, the physical/structural origin for such a size effect is not well understood at the present time, and still remains an important ongoing research topic. In summary, it has been demonstrated that TFMGs possess high mechanical strength because of their amorphous structure, and good ductility owing to their small thickness. Such a unique integration of mechanical properties renders TFMGs promising materials for a variety of engineering applications [10,38,62,63] in recently emerging MG-based micro- and nano-technology that have already attracted research interest [60,62,63].

3.6.4. Multilayered TFMGs

In addition to monolithic films, multilayered TFMGs have attracted attention in recent years. For mechanical property improvement, multilayered systems consisting of thin layers of nanocrystalline metal and metallic glass are prepared [64–68]. The metal layer should be sufficiently strong in modulus and strength while being deposited with the appropriate film orientation. Face centered cubic Cu(111) films appear to be too soft, whereas body-centered cubic Mo(110) films are too brittle. Hexagonal close-packed Zr(001) matches the above requirements [65,68]. During deformation of multilayered TFMGs, the shear bands initiated in the TFMG layer can be absorbed and accommodated by the nanocrystalline Zr(001) layer via nano-twinning. Zr-based-TFMG/Zr multilayers can be highly ductile with semi-uniform plastic deformation of 55%. They are even more ductile than many pure metals, as shown in Fig. 18 [68]. The amorphous-crystalline interface exhibits good strain compatibility after appreciable plastic deformation.

Another example is Zr-based-TFMG/crystalline-Ta multilayers. FIB-machined multilayer micro-pillars have been evaluated by micro-compression tests [37], as shown in Fig. 19. Compared with monolithic Zr-based-TFMG pillars, the TFMG/Ta multilayer pillars exhibit considerably higher yield stress as well as improved deformability. The enhanced mechanical properties are attributed to positive effects from high-stiffness Ta layers, which are not involved in formation of shear bands, but can retard shear band propagation by forming a "plastic zone" in the constrained Zr-based-TFMG layers.

The tensile behavior of multilayer TFMGs has been also reported. Monolithic Zr-based TFMGs and Zr-based-TFMG/Cu multilayer coatings on pure Cu foils have been examined [69]. The extracted tensile modulus and strength of 1-μm-thick multilayers are in good agreement with rule-of-mixtures predictions. The results reveal that the multilayer coatings exhibit much better tensile performance than monolithic TFMGs, despite the brittle deformation.

In addition to nanocrystalline metal interlayers, TFMG interlayers of different composition have also been used to form TFMG/TFMG

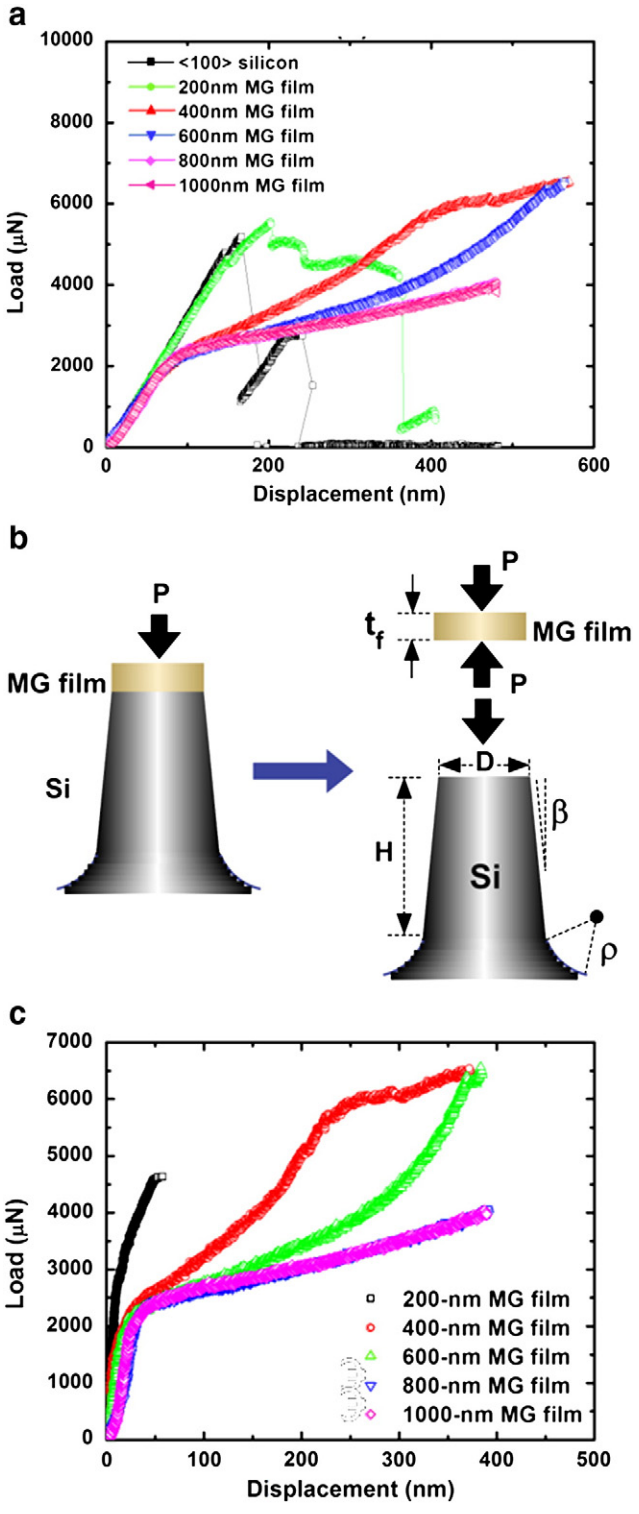

Fig. 16. (a) Load-displacement curves obtained from TFMG-coated Si(001) micropillars with pillar diameters ~1 μm, height ~3 μm, and the taper angle ~2°, (b) a schematic illustration demonstrating the method for extracting the mechanical properties of the TFMG by subtracting the mechanical response of the Si substrate from the total response; and (c) extracted load-displacement curves for the $Zr_{53}Cu_{29}Al_{12}Ni_6$ TFMGs.

multilayered structures [70,71], as shown in Fig. 20. An example is the Zr-based-TFMG/Pd-based-TFMG multilayered system, whose uniaxial microcompression and nanoindentation responses have been investigated [70]. It is found that the apparent deformation mechanism transforms from a highly inhomogeneous mode in monolithic amorphous alloys to a more homogeneous mode in micropillars of TFMG/TFMG

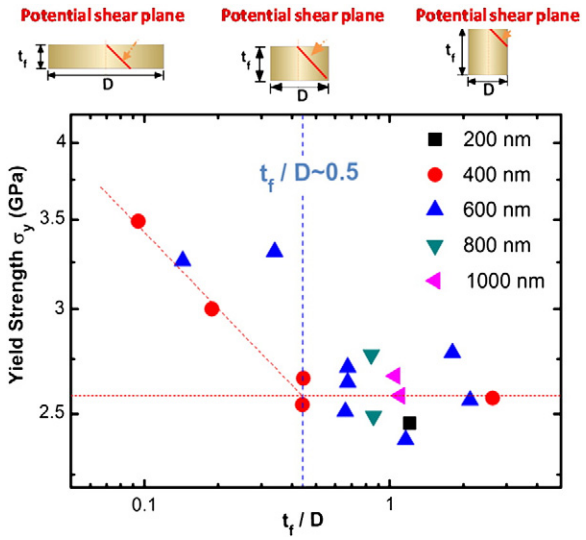

Fig. 17. The shape dependence of the yield strengths obtained from $Zr_{53}Cu_{29}Al_{12}Ni_6$ TFMGs of different aspect ratios (the insets on the top illustrate the aspect-ratio effect on shear band formation). t_f is the film thickness and D is the substrate diameter.

multilayers. Similar phenomena were observed under nanoindentation. The presence of sharp amorphous/amorphous interfaces, which could hinder the propagation of shear bands, is a possible reason for the observed transition in the deformation mode.

3.7. Adhesion and tribological properties

Among the mechanical properties of TFMGs, there are few reports of adhesion and tribological properties [24,72,73]. In general thin film technology, scratch adhesion tests are frequently used for coating evaluation. Qualitative and quantitative information about the adhesion of a coating to a substrate can be obtained from nano/micro/macro scratch experiments. A scratch test provides not only the critical load to failure, but also the type of failure mode [74–76].

For BMGs, the scratch resistance of Mg-based-BMGs has been evaluated using a nanoindenter with a Berkovich probe [77]. The wear mode changed from rubbing and/or ploughing to cutting as the normal load was increased from 5 to 200 mN. The tribological properties of Zr-based BMGs have been examined using ramping-load nanoscratch and multiple-sliding nanowear techniques [78]. The best wear performance is obtained for structures consisting of an amorphous matrix with dispersed nanocrystalline particles. A study of the tribological behaviors of Ce-, Ti- and Fe-based BMGs by ramping-load nanoscratch tests reported that higher hardness correlated with better scratch resistance [79].

The tribological behavior of Zr-based TFMG ($Zr_{47}Cu_{31}Al_{13}Ni_9$) deposited on 316 L stainless steel, probed using the micro-scratch technique, was reported by Liaw et al. [73]. For this TFMG, a penetration depth profile, the coefficient of friction (COF) during the scratch test, and an SEM image of the scratch track after ramp-loading of 25–250 mN are shown in Fig. 21 [73]. The critical load is determined to be 110 mN and is marked with a vertical arrow. The average COF value was 0.23 at a 100 mN normal load. When the normal load increased to 300 mN, the COF value increased to ~0.62. The scratch tracks near the film failure area are shown in the SEM micrographs of Fig. 22 [73]. It is clear that a high density of shear bands is formed along the sliding direction. However, no obvious debonding is observed. The smooth scratch groove and the small shear band spacings indicate a ductile deformation mode with good film plasticity. For sputtered Zr-based-TFMGs on stainless steel substrates, Jang et al. found that adhesion increased with sputtering power to a saturated critical scratch-test load of 70 N [72]. Conversely, poor adhesion properties of sputter-deposited Pd-based TFMGs on Si(001) substrates have also

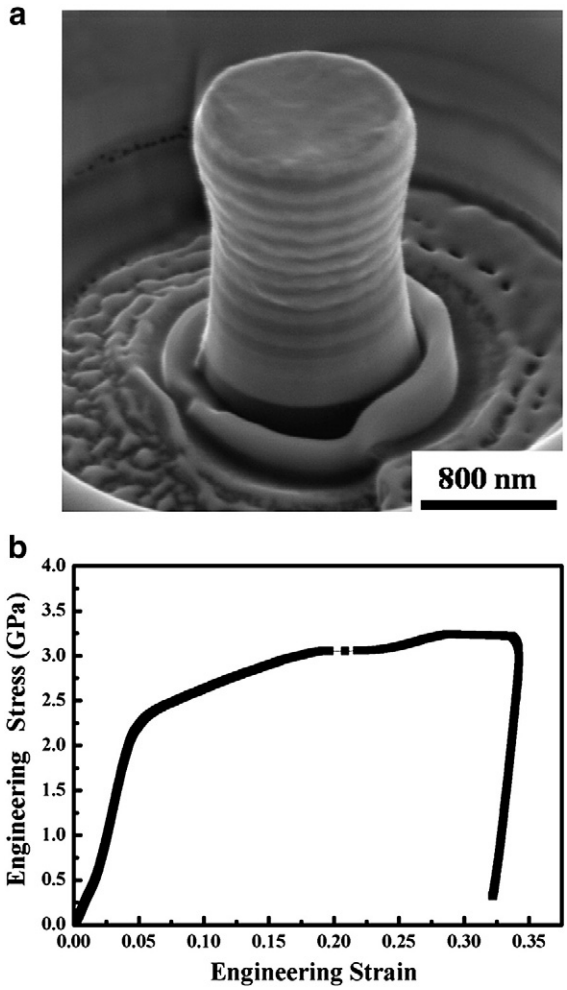

Fig. 18. (a) SEM micrograph showing a TFMG/Zr (100/100 nm) multilayer on Si(001) pillar compressed to a predetermined displacement of 500 nm (~25% strain), and (b) the recorded engineering stress/strain curve.

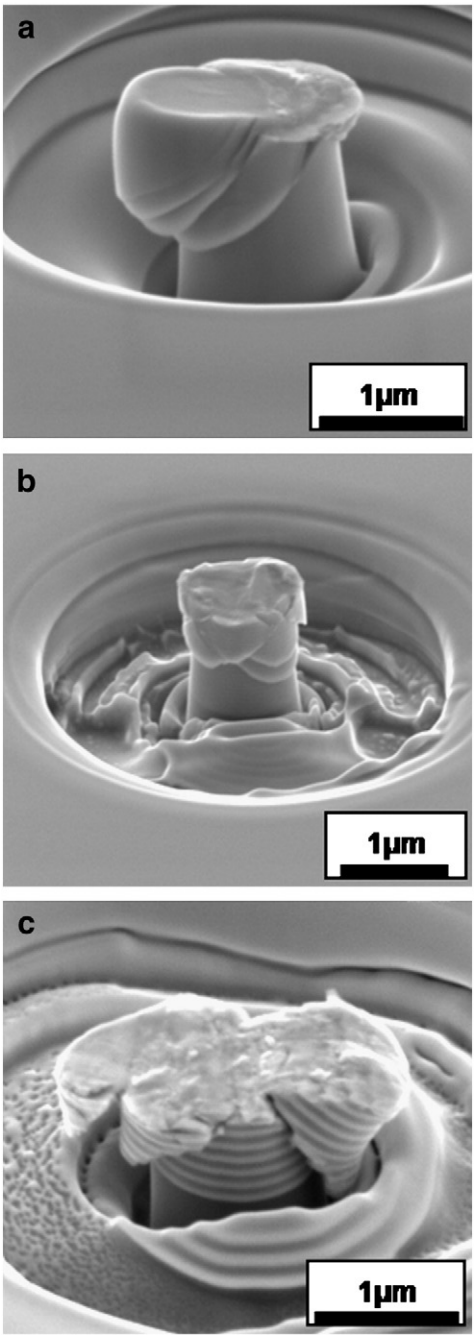

Fig. 19. SEM micrographs (a) monolithic Zr-based TFMG (b) Zr-based TFMG/Ta (50/5 nm) multilayer, and (c) Zr-based TFMG/Ta (50/50 nm) multilayer on Si(001) pillars deformed by micro-compression [37]. The pillars, 900 nm in diameter by 1500 nm high, were formed using an FIB.

been reported [24]. Hence, the adhesion properties of TFMGs show wide variations with composition, deposition technique, and substrate.

In recent work, a 210-nm-thick Zr-based TFMG ($Zr_{58}Cu_{25}Al_{11}Ni_6$) deposited on Si(001) by pulsed DC magnetron sputtering [80], with a synchronous pulsing bias of −50 V applied to the substrate, has been evaluated for adhesion and tribological properties. The adhesion behavior was examined using a scratch tester with the normal load from 0.1 to 50 N and scratch lengths of 5 mm. Fig. 23 illustrates the coefficient of friction (COF) and friction force versus scratch length, together with SEM images of surface morphologies of scratch tracks. It is clear that the mean COF value was around 0.3–0.4. This result is similar to that of $Zr_{47}Cu_{31}Al_{13}Ni_9$ metallic glass films on Si(001) reported by Liaw et al. [73]. No apparent crack or delamination was found adjacent to the scratch track of the coating, suggesting good adhesion.

3.7.1. Rockwell-C adhesion test

The Daimler–Benz Rockwell-C (HRC-DB) adhesion test [81] is an easy and commercially adopted method to evaluate film/substrate adhesion quality. A load of 1471 N is applied to cause film damage, and the degree of the damage is classified into six grades, HF1–HF6. In general, the adhesion strength quality HF1 to HF4 defines sufficient adhesion, whereas HF5 and HF6 represent poor adhesion in the HRC-DB test. The adhesion of $Zr_{55}Cu_{27}Al_{12}Ni_6$ TFMGs deposited on tool steel (SKD 61) substrates by pulsed-DC magnetron sputtering has been evaluated by using Rockwell-C adhesion tests and compared to results for CrN [82] and TiN films [83] deposited on SKD 61 and high speed steel substrates, respectively, by the same method. The film thickness, hardness, and elastic modulus of TFMG, CrN and TiN films are listed in Table 2. As expected, the TFMG, due to its metallic nature, has lower hardness and modulus than those of hard ceramic CrN and TiN films. The HF values obtained from the HRC-DB test listed in this table reveal excellent adhesion; HF1 for all films examined. Different surface morphologies are observed in SEM micrographs (Fig. 24) obtained from the indentation craters after the adhesion tests. For the TFMG, there is negligible radial cracking and film delamination; however, brittle fracture features are observed for both the CrN and TiN films. The brittle features include many circular bulge wrinkles adjacent to the crater in CrN and a number of brittle cracks emanating radially from the crater in TiN. This suggests that the Zr-based TFMGs exhibit good adhesion to steel

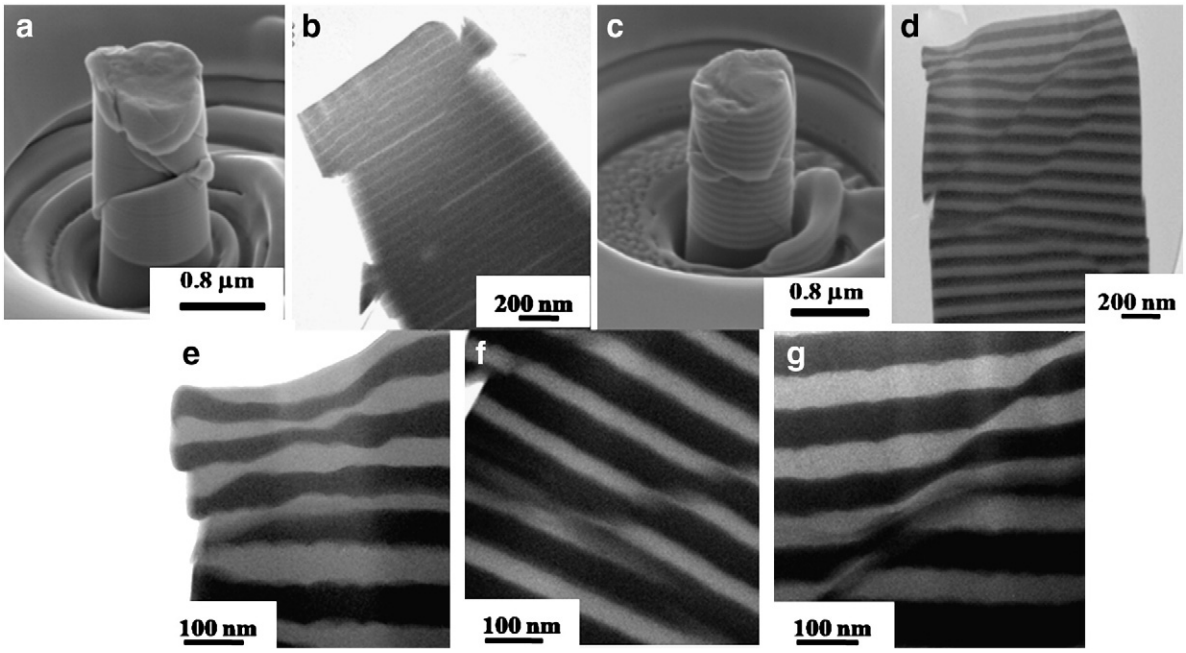

Fig. 20. Electron micrographs showing MG/MG multilayers on Si(001) pillars compressed to a displacement of 300 nm. SEM: (a) 5/50 nm Zr-based MG/Pd-based MG system, and (c) 50/50 nm Pd-based MG/Zr-based MG system. TEM: (b) 5/50 Zr-based MG/Pd-based MG, (d) 50/50 Pd-based MG/Zr-based MG. Higher resolution views of sample (d): (e) upper left corner, (f) upper center, and (g) layer deformation due to shear band propagation [70].

with better ductility than ceramic hard coating films. A similar result has been obtained when TFMGs and the hard coating (such as TiN) are deposited on BMG surfaces for a comparison study, in which TFMGs are found to exhibit ductile feature whereas TiN is brittle [84].

3.7.2. Wear resistance

Wear resistance plays an important role in many applications. For BMGs, much effort has been devoted to examining tribological properties. Ni-based BMG micro-gears have longer lifetimes than micro-gears made of steel [85]. The wear resistance and hardness of Zr-based BMGs increase with increasing Ag content over the range from 2 to 8 at.% [86]. A study of the tribological behavior of the B_4C-reinforced Fe-based BMG plasma-sprayed coatings reveals that the observed reduction in wear loss, hardness increase of the wear surface, and inhibited plastic flow propagation are largely due to the incorporated hard material, B_4C, in the amorphous coating [87]. The tribological behavior of the

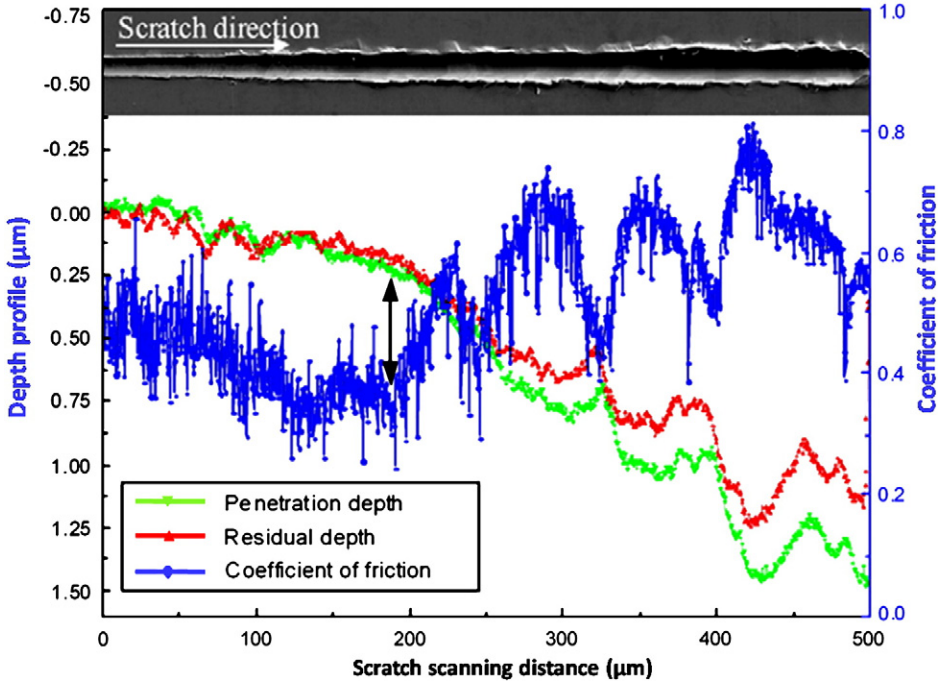

Fig. 21. Penetration depth and COF vs. the scratch distance along a Zr-based TFMG on 316 L stainless steel for ramp loading of 25–250 mN [73]. SEM micrograph taken from the test region is shown above the graph.

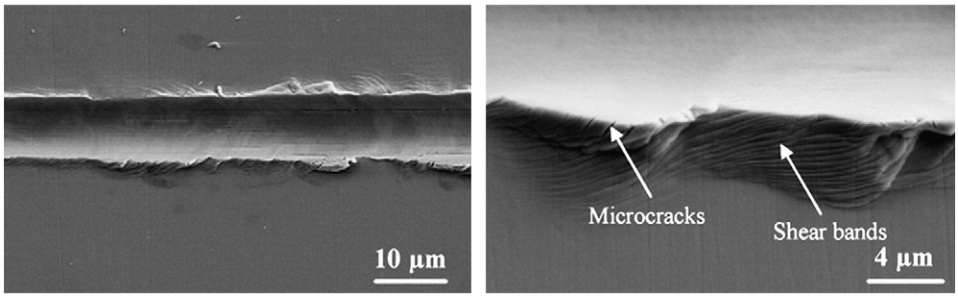

Fig. 22. SEM micrographs of scratch tracks along a Zr-based TFMG on 316 L stainless steel under a ramp load of 25–200 mN at (left) lower and (right) higher magnifications [73].

porous and WC particle-containing Fe-based TFMG coating layers has been explored, revealing excellent tribological and wear characteristics, attributable to the amorphous matrix [88].

However, a fundamental understanding of tribological properties of TFMGs is still lacking. Recent research on the wear resistance of Zr-based TFMGs deposited on SKD 61 steel using pulsed DC magnetron sputtering has been carried out. A pin-on-disk wear method was used to investigate the wear resistance. A SiC ball, 6 mm in diameter, was adopted as the stationary pin with a normal load of 1 N. The sliding speed was 9.8 mm/s with a wear track diameter of 6 mm and a wear length of 20 m. Fig. 25 shows the COF versus wear length for both the TFMGs and the bare steel substrate. It was found that the film was almost worn through at a wear length ~6.8 meters as the COF values of film and substrate merged. The wear scar morphology of the film after the pin-on-disk wear test for a wear length of ~228 μm is shown in the SEM micrograph in Fig. 26. No obvious debonding is found, but plastic deformation can be observed in many areas. Plastic deformation of the wear track might have caused a higher COF value for the TFMG in this case.

4. Potential applications

4.1. TFMGs for biomedical use

4.1.1. Antimicrobial

Nosocomial infection frequently occurs in hospitals. The infection is found to be caused by transmission of pathogens from the hospital environment (such as instruments or equipment) and by direct hand-to-hand contact between health-care providers and patients [89]. The most common causative pathogens have been reported as *Staphylococcus aureus*, *Escherichia coli*, *Pseudomonas*, and mixed-microbial infections [90,91]. In addition, *Acinetobacter baumannii* is another important pathogen in recent years [92,93]. Generally, stainless steel is used for many medical environmental surfaces such as door handles and push plates, and also in many different devices such as surgical instruments [91,94].

Michels et al. [95] reported that copper alloys or copper-containing materials exhibit high efficacy levels as antimicrobial materials at temperature and humidity levels typical of indoor environments, such as hospitals. Therefore, surface conditions of stainless steel located at possible hand-contacting regions (door handle, push plate) can be modified by adding a thin coat of hard, smooth Cu-containing film such as Zr-based TFMGs ($Zr_{61}Cu_{17.5}Ni_{10}Al_{7.5}Si_4$), which improve antimicrobial properties [72]. This TFMG has good hydrophobic properties, with a wetting angle of 92° compared to 46° for 304 stainless steel. Additionally, the films have extremely smooth surface profiles (roughness ~1 nm) and a homogenous composition distribution while exhibiting strong antimicrobial effects for different microbes including *E. coli*, *S. aureus*, *Pseudomonas aeruginosa*, *A. baumannii*, and *Candida albicans* for at least 24 h as shown in Fig. 27 [72]. More recently, Jang et al. have reported a Ag-containing Zr-based TFMG [$(Zr_{42}Cu_{42}Al_8Ag_8)_{99.5}Si_{0.5}$], also deposited by sputtering on stainless steel surfaces [96]. The 500-nm-thick films have physical properties similar to Zr-based TFMGs: surface roughness (<1 nm), hardness (~6 GPa), adhesion (~70 N load), and amorphous structure as characterized by XRD and TEM (see Fig. 28). However, the Ag-containing TFMGs exhibit much better antimicrobial capabilities, as shown in Fig. 29. No microbe growth of *E. coli*, *C. albicans* and *S. aureus* is found on surfaces coated with Ag-containing TFMGs after 76 h.

4.1.2. TFMGs for medical tools

Potential applications of Zr-based TFMGs can be extended to medical tools such as surgical blades and micro-surgery scissors. Commercial blades made of martensitic stainless steel always present micron-scale roughness on the edge surface and edge tip [97]. This rough blade edge directly influences the blade sharpness as well as the surgical quality, and eventually the performance and life of the tool. The sharpness of a blade is a key parameter in cutting soft solids,

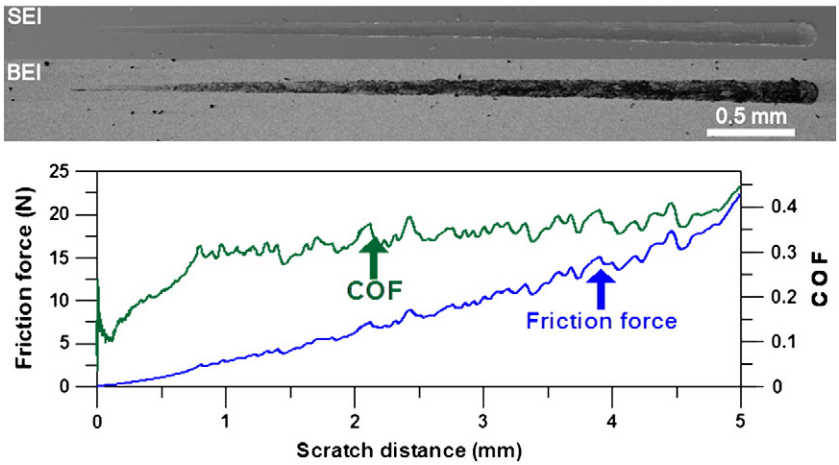

Fig. 23. (Upper) SEM micrographs in secondary electron (SEI) and backscattered electron (BEI) modes and (lower) friction force and COF vs. the scratch distance along a Zr-based TFMG on Si(001).

Table 2
Film thickness, hardness, elastic modulus and adhesion of $Zr_{55}Cu_{27}Al_{12}Ni_6$ TFMG, CrN [79], and TiN [80] layers.

Films	Thickness (nm)	Hardness (GPa)	Elastic modulus (GPa)	Adhesion strength quality (HF value)
Zr-based TFMG	500	5.9 ± 0.1	109.2 ± 2	1
CrN	1500	22.2 ± 3.8	239.7 ± 26.3	1
TiN	3000	32 ± 4	470 ± 50	1

such as biological tissues or elastomeric materials, and it is related to the energy required to cut, the quality of the cut surface, and the life of the cutting instrument. In addition, the depth of blade indentation necessary to initiate a cut or crack in the target material is a function of sharpness of the blade's cutting edge, characterized by the "blade sharpness index" (BSI) [98]. BSI is defined as $\int_{\delta_i} Fdx/\delta_i t J_{Jc}$ and illustrated in Fig. 30, where F is the applied force, dx the increment of blade displacement, δ_i the initial depth of blade indentation before test material fracture, l the length of cut surface, J_{Ic} the Mode I fracture toughness (crack opening directly to two sides), and t the thickness of test material. The index is zero for an infinitely sharp blade and increases with bluntness in a quadratic manner.

The blade sharpness index BSI of a commercial stainless steel blade (Surgical Blade No.11, FEATHER Safety Razor Co.) with and without sputter-deposited Zr-based TFMGs has been evaluated by cutting a rubber material (styrene-butadiene rubber, SBR) in a specially-designed test rig (see Fig. 31). The setup is mounted on a 50 kN universal testing machine for measuring the applied force. The SEM results in Fig. 32 [96] clearly show that the surface roughness of a commercial scalpel (with ~1.2 μm average roughness) can be significantly decreased to ~0.4 μm by coating it with a 200-nm-thick $Zr_{53}CuNiAlSi$ TFMG. The coating also decreases the BSI value from ~0.36 to ~0.25, a 26.5% improvement in sharpness.

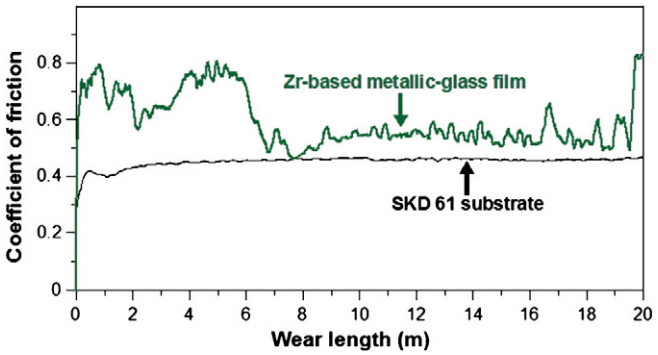

Fig. 25. The coefficient of friction of a 500 nm-thick Zr-based TFMG/steel sample and the bare substrate against a SiC ball as a function of wear length.

4.2. Improved fatigue properties due to TFMGs

Beneficial effects of TFMGs on fatigue-properties of crystalline metallic substrates have been reported and some important results are summarized in this section. The TFMGs investigated to date are primarily sputter-deposited $Zr_{47}Cu_{31}Al_{13}Ni_9$, $Cu_{51}Zr_{24}Hf_{18}Ti_7$, and $Fe_{65}Ti_{13}Co_8Ni_7B_6Nb$ on substrates including stainless steels [38,99], Ni- [100], Al- [96], and Ti- [101] based alloys. Substrates are polished with fine grits, or electropolished, prior to TFMG deposition. The coated substrates are then subjected to tension during four-point bending fatigue tests at room temperature. The experiments are conducted with an R ratio of 0.1, where $R = \sigma_{min}/\sigma_{max}$, in which σ_{min} and σ_{max} are the applied minimum and maximum stresses, respectively, at a frequency of 10 Hz.

The first known study reporting fatigue property improvement was for 200-nm-thick Zr-based TFMG coated 316 L stainless steel substrates [38]. The stress versus number of fatigue cycles to failure

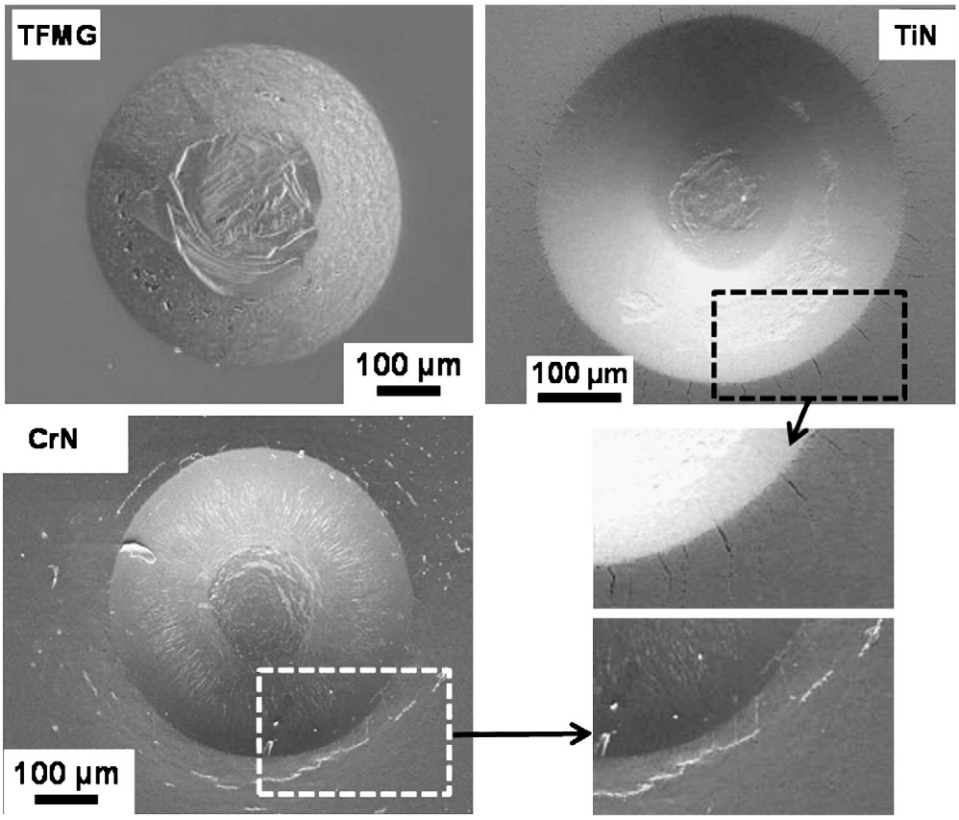

Fig. 24. SEM micrographs of indent craters in Zr-based TFMG/SKD61, CrN/SKD61 [82], and TiN/HSS samples [83] following Rockwell-C adhesion tests.

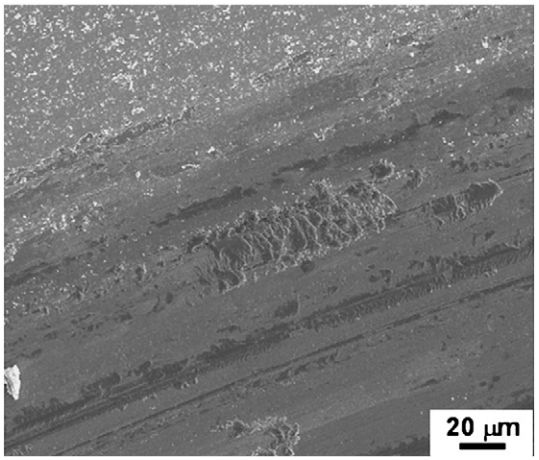

Fig. 26. SEM micrograph showing wear scar morphology of a 500 nm-thick Zr-based TFMG/steel sample during a pin-on-disk wear test.

(S–N) curve of the 316 L stainless steel with and without TFMGs is presented in Fig. 33 [38]. The fatigue life of the coated samples is increased by 30× over that of the bare substrate and the fatigue limit is enhanced by up to 30%, depending on the maximum stress applied. Fatigue improvements are not always this high. For instance, fatigue life improvement is only ~4× at 650 MPa, with the fatigue limit enhanced significantly by 53% from 400 to 600 MPa (Fig. 34), for Ni-based substrate coated with Zr-based TFMGs [100].

Fatigue improvements are attributed to several factors such as higher strength and ductility of the TFMG. In addition, a smooth surface is obtained with the TFMG coating, which is beneficial for decreasing crack formation during fatigue testing. As will be discussed subsequently, both excellent adherence and the smooth film surface influence the fatigue life of the TFMG/substrate system.

4.2.1. Governing mechanisms

It is proposed that during fatigue testing, dislocation pileups or persistent slip bands, when arriving at the surface, can create a surface offset on the substrate, which becomes a potential fatigue-crack-initiation site. Hence, the substrate surface normally becomes rough during

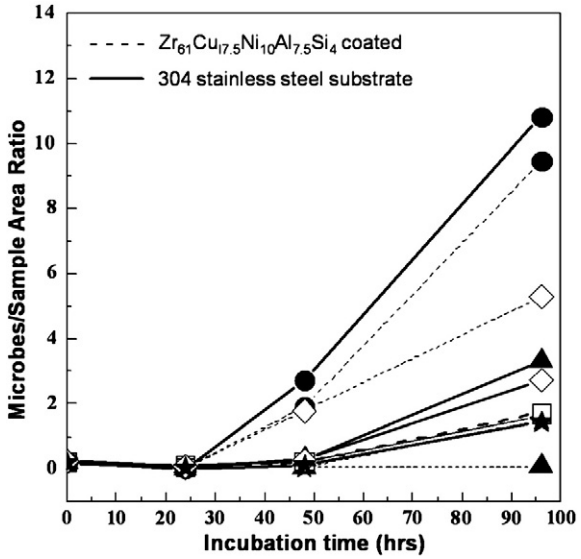

Fig. 27. Microbes/sample area as a function of incubation time on Zr-based TFMGs/steel and the bare substrate for different microbes growing in a Mueller-Hinton agar plate. *Escherichia coli* (▲), *Staphylococcus aureus* (□), *Pseudomonas aeruginosa* (●), *Acinetobacter baumannii* (◇), and *Candida albicans* (★) [72].

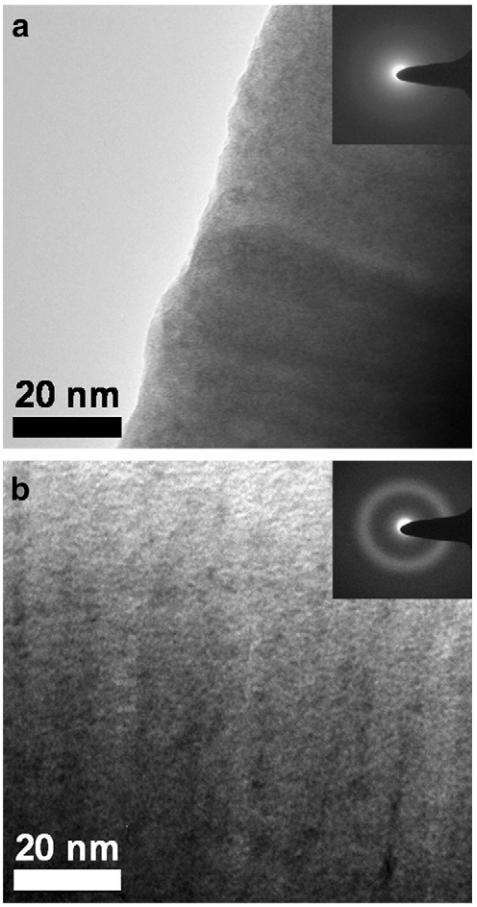

Fig. 28. Cross-sectional bright-field TEM images, with selected area diffraction patterns (insets), of TFMGs on Si(001) substrates: (a) $(Zr_{53}Cu_{30}Ni_9Al_8)_{99.5}Si_{0.5}$ and (b) $(Zr_{42}Cu_{42}Al_8Ag_8)_{99.5}Si_{0.5}$.

fatigue testing, mostly caused by the formation of offsets at film/substrate interfaces, as shown in a SEM micrograph of Fig. 35(a) for a 200-nm-thick $Zr_{53}Cu_{29}Al_{12}Ni_6$ TFMG on 316 L stainless steel following a four-point-bending fatigue test to failure [102]. It is worthwhile to examine the effect of TFMG coatings on these offsets. In this case, a Zr-based TFMG is well adhered on the offset area with a pimple-like appearance on the film surface. The offsets are mainly caused by slip bands propagating in the crystalline substrate as shown in the TEM image of Fig. 35(b). As a result of the slip-band formation, a hump is clearly seen at the substrate surface. In Fig. 35(c), the TEM image reveals columnar grains in the film. The columnar grains may have slipped to cause the pimple-like appearance on the surface. This observation confirms that the film is ductile enough to accommodate substrate deformation during cyclic loading. Of course, some parts of the film eventually are peeled off at the film/substrate interface upon large deformation or increased fatigue life cycles, as shown in Fig. 35(d). The film thickness effects on the fatigue property of the 316 L stainless steel substrate have been also studied using Zr- and Cu-based TFMGs [99]. An example for Zr-based TFMGs is shown in Fig. 36 [99]. In the figure, the improvements in both fatigue limit and life are more pronounced for the 1-μm-thick than the 200-nm TFMG film. The improvements are considered to be due to greater suppression of surface offsets by the thicker film on the substrate.

In coated materials, surface-crack initiation plays a major role in controlling sample fatigue life when the sample is subjected to high-cycle fatigue. Fatigue-resistance enhancement is thought to be due primarily to lifetime extension during the fatigue-crack-initiation stage. Once a fatigue crack propagates, the thin-film coating clearly has little influence. SEM fractographs of a fatigue-fractured stainless steel substrate coated

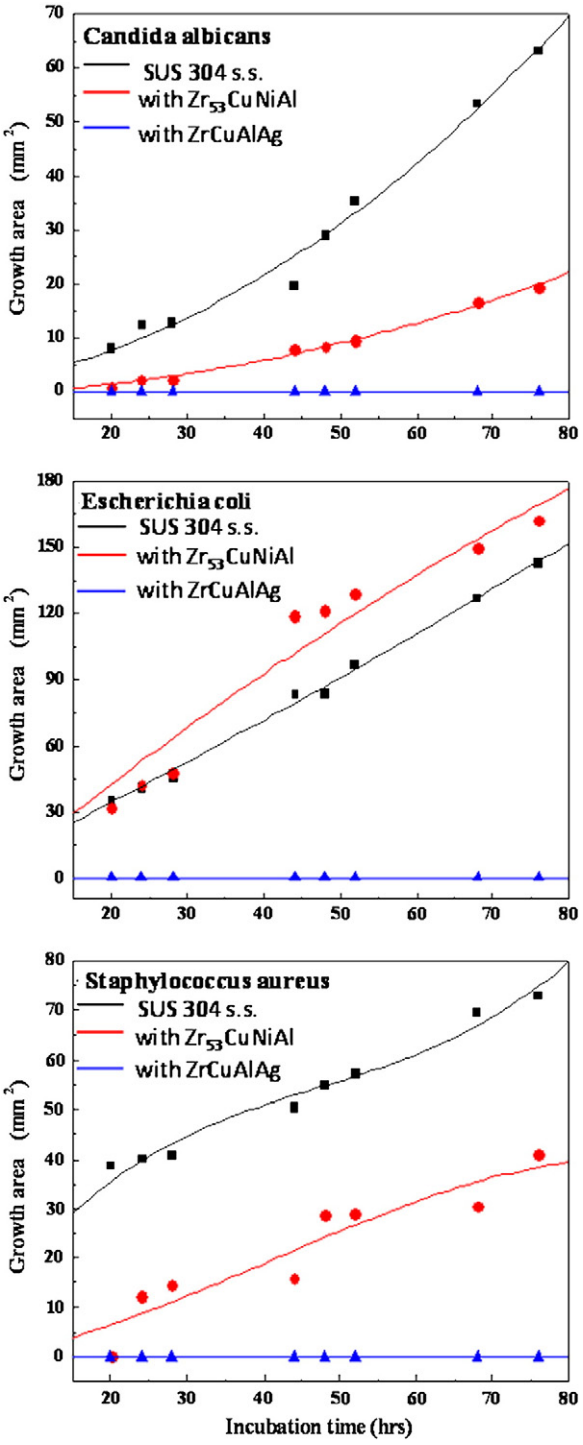

Fig. 29. Bacterial growth analyses results for SUS304 stainless steel substrates and substrates coated with $(Zr_{53}Cu_{30}Ni_9Al_8)_{99.5}Si_{0.5}$ (Zr_{53}CuNiAl) and $(Zr_{42}Cu_{42}Al_8Ag_8)_{99.5}Si_{0.5}$ (ZrCuAlAg) TFMGs: (upper) *Candida albican*, (middle) *Escherichia coli*, and (lower) *Staphylococcus aureus*.

with a 200 nm-thick Zr-based TFMG are presented in Fig. 37. Fatigue-crack-initiation and crack-propagation regions are observed on the substrate fracture surface in Fig. 37(a). The crack appears to initiate from the substrate surface and then grow into the substrate. The arrows in the micrograph indicate the crack-propagation direction. Fatigue is surface-sensitive and can be improved by the deposition of a coating to suppress crack initiation at the substrate surface. A tilted view image in Fig. 37(b) indicates that even after severe plastic deformation

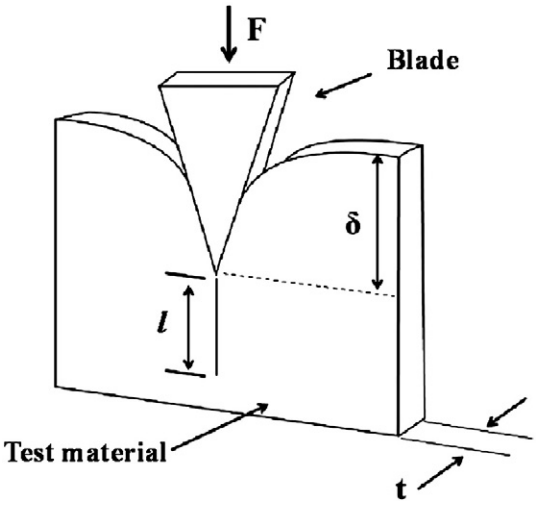

Fig. 30. Illustration of the indentation cutting process used for evaluating the blade sharpness index (BSI) [98].

and final fatigue fracture, the film remains well adhered with the substrate. No cracks are observed on the film.

4.2.2. Annealing effects

For further improvements, coated 316 L stainless steel substrates are thermally annealed within ΔT, the temperature range between glass-transition and crystallization temperatures, using a rapid thermal annealing system. The holding time is limited to 1 min to minimize softening of the substrate surface. Fig. 38 shows the S–N curves of 316 L stainless steel substrates coated with as-deposited and annealed Zr-based TFMGs [99]. Both as-deposited and the annealed samples exhibit better fatigue resistance than the bare substrate. With a stress of 750 MPa, the fatigue life is increased ~10×, from 4.4×10^5 cycles for the uncoated sample to 4.5×10^6 cycles for the as-deposited one. The life is improved further by 22×, $>10^7$ cycles, for the annealed sample due to the fully amorphous TFMG microstructure after annealing.

The film surface morphology is also affected after annealing within ΔT, as described previously (Section 3). In general, sample surfaces are reported to become smoother when TFMGs are deposited [38,96,100,102,103], as shown in Fig. 39(a) and (b) [102] where the surface roughness of a stainless steel substrate decreases from 4.6 nm to 2.3 nm after deposition of 200 nm-thick $Zr_{53}Cu_{29}Al_{12}Ni_6$ films. The roughness further decreases to 1.2 nm after the coated substrate is annealed within ΔT for 1 min [Fig. 39(c)]. This annealing-

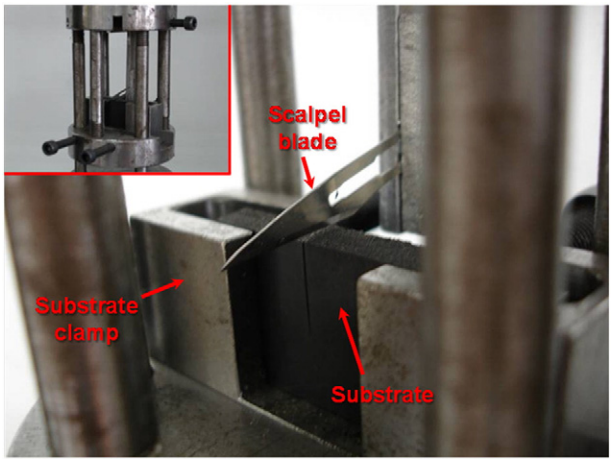

Fig. 31. Experimental setup used for evaluating the blade sharpness index (BSI) of a cutting tool (inset: the entire apparatus).

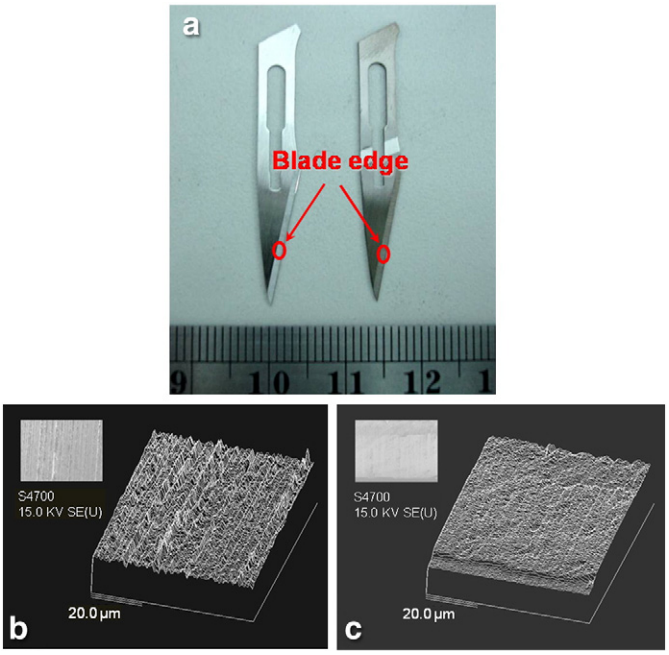

Fig. 32. (a) (Left) bare and (right) Zr-based TFMG-coated commercial blades; red circles are the regions used to obtain the SEM images in (b) and (c). SEM images and surface profile scans of edge regions for (b) bare and (c) coated samples [96].

induced amorphization [similar to Fig. 3] plays an important role in surface smoothening. Rough surfaces are thought to facilitate crack initiation and are not favorable for good fatigue performance. Annealing of conventional metallic films results in adverse softening and rough surfaces due to grain growth, whereas brief annealing of TFMGs within ΔT has many beneficial effects. A fully amorphous structure and dense TFMG film microstructure after annealing can be achieved, as shown in Fig. 40 [102]. Annealing-induced amorphization is clearly observed in Fig. 40(a) and (b). After annealing, the structure becomes more homogeneous and columns are absent [Fig. 40(d)]. The annihilation of the column structure is primarily due to vitrification [102].

4.3. TFMGs for bendable bulk metallic glass

Bulk metallic glasses (BMGs) have attracted enormous interest due to their exceptional properties as mentioned in Section 1. However, applications of BMGs have, until now, been severely limited by the prevalence of brittle fracture upon deformation at room temperature. The lack of ductility is mainly due to the detrimental formation of a few large localized shear bands, leading to the catastrophic fracture [104,105]. There have been several approaches to improve the room-temperature ductility in BMGs, including microstructure modification by forming composite structures in the amorphous matrix [106,107] and surface modifications such as thick (~90 μm) coatings [108]. It has been demonstrated, for the first time, that a thin, strong, ductile, and adhesive coating renders BMGs bendable at room temperature [84]. The four-point bending ductility (surface strain) of 3-mm-thick BMGs ($Zr_{50}Cu_{30}Al_{10}Ni_{10}$) can be significantly enhanced from ~0 to ~13.7% by the deposition of a thin bilayer film on the tensile side of the BMG sample. This enhancement is demonstrated in both bending stress-strain curves and photographs in Fig. 41. The bilayer, consisting of a 25-nm-thick Ti adhesive layer with a 200-nm-thick TFMG ($Zr_{53}Cu_{26}Al_{15}Ni_6$) overlayer, exhibits the required combination of good adhesion, high strength, and ductility compared with other single-layer films examined (Ti, TiN, and TFMG) [84]. Experimental and numerical modeling results suggest that during bending deformation, the bilayer coatings partially absorb the deformation energy, decrease the number of initiating points due to flaws at the uncovered BMG surface, and allow the formation of a high-density of more homogeneously distributed shear bands [84]. The idea of using a thin coating to modify and improve the mechanical properties of BMGs is interesting and suggests that the room-temperature ductility of BMGs is a surface-sensitive property.

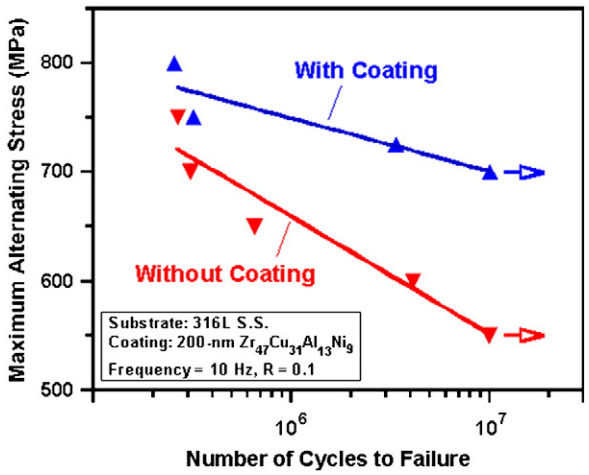

Fig. 33. Stress-lifetime (S–N) curves for bare 316 L stainless steels with and without Zr-based TFMGs after four-point bending fatigue tests to failure [38]. Arrows indicate run-out data without failure.

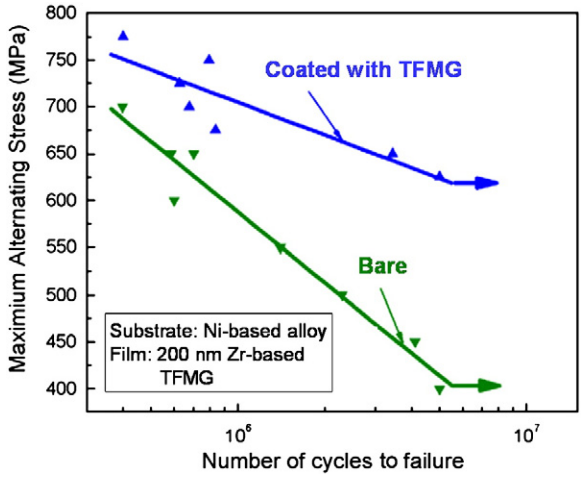

Fig. 34. Fatigue S–N curves for Ni-based alloys with and without Zr-based TFMGs. Arrows indicate the run-out data without failure [100].

4.4. Micro and nano replication

Replication of devices, parts and patterns with features in micro- and nano-size scales can be done by imprinting features from a hard mold. The imprint process promises low fabrication costs for materials and allows mass production. In addition to excellent mechanical properties, such as high room-temperature strength, BMGs exhibit viscous flow at temperatures within ΔT and unusually low thermal expansion. Thus, they are malleable for forming micro- and nano-scaled parts with complex shapes because of the extremely uniform flow properties, *i.e.* superplasticity. The main advantages of using BMGs, over conventional crystalline materials, for the replication of micro- and nano-sized features include high strength, excellent wear and corrosion resistance, low process force, ease of demolding, good surface quality, and intrinsic homogeneity at the nanoscale due to the absence of grain boundaries. Hence, replicated BMG components are being used as molding dies to further create second-generation replicas in conventional polymethylmethacrylate (PMMA) [109,110].

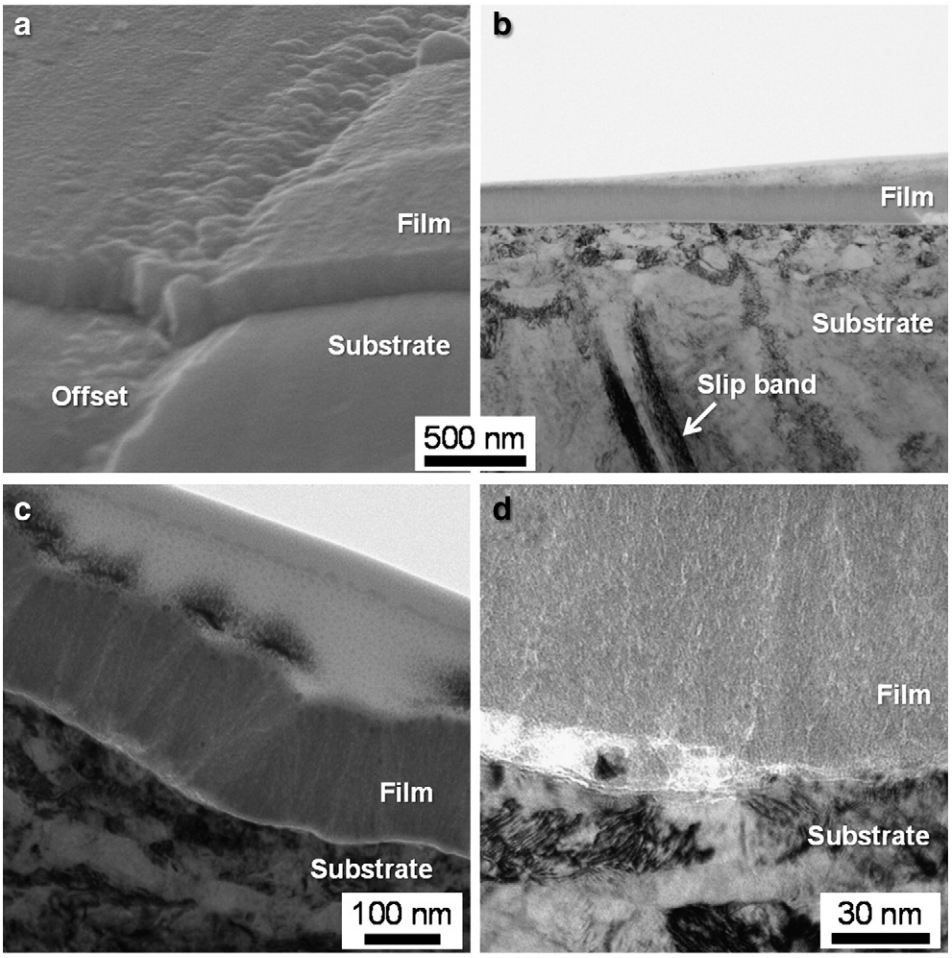

Fig. 35. (a) SEM image of the offset on the tension surface of a 200-nm-thick-TFMG-coated stainless steel substrate after a fatigue test to failure. Cross-sectional TEM images from the same sample showing: (b) slip bands formed in the substrate, (c) an offset area covered with the Zr-based TFMG, and (d) a film delamination region [102].

There are many reports on micro- and nano-scale forming for BMG parts [63,109–113]; yet, very few investigations on TFMGs have been performed. The replication of TFMGs in the nanoscale remains challenging from both the scientific and engineering points of views. One of the key issues, for instance, is that the film is not necessarily uniform in 3D and is not free from defects, because of the presence of columnar structures such as the ones shown in Figs. 4 and 11. Also, the nature of the film geometry makes it increasingly more difficult for TFMGs to fill extremely fine features with high aspect-ratios as device sizes in MEMS or NEMS decrease to the sub-micrometer and nanometer regions. Therefore, micro and nano replications of TFMGs are normally limited to surface or planar geometries. The following are some TFMG examples that have been reported for MEMS and NEMS applications.

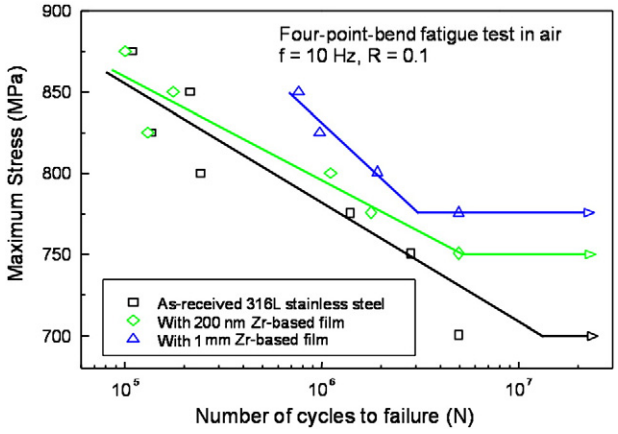

Fig. 36. Fatigue S–N curves of bare 316 L stainless steel and samples coated with different thicknesses of Zr-based TFMGs [99]. Arrows indicate run-out data without failure.

Although it was not processed by replication within ΔT, a Pd-based ($Pd_{76}Cu_7Si_{17}$) TFMG was one of the first to be used to form an integrated conical spring linear actuator (CSLA). In this MEMS-type device, the CSLA can be lifted as an actuator when the temperature is raised within ΔT [114].

To evaluate formability within ΔT, several TFMG systems (Zr-, Pd-, and Cu-based) are deposited by sputtering, followed by thermal imprinting tests using Si and ZnMnO nanodot array molds [115–118]. The results suggest that the imprinted hole pattern depth in TFMGs increases with processing temperature and the low viscosity yields a large hole depth. For example, the maximum hole depths of imprinted 100 nm-thick Zr-, Cu-, and Pd-based TFMGs are 49, 63 and 88 nm, corresponding to viscosity values of 1.1×10^9, 8.8×10^8, and 4.5×10^7 Pa-s, respectively [117]. Thus, the TFMG with the lowest viscosity within ΔT is most easily deformed during the replication process.

The low wettability of TFMG is another important property, particularly for the demolding stage. Furthermore, a wide ΔT range is preferred because of the large temperature window for better process control. Among many TFMGs, Pd-based systems with large ΔT, low viscosity, and good wettability exhibit excellent deformability for nano-structure replications [117].

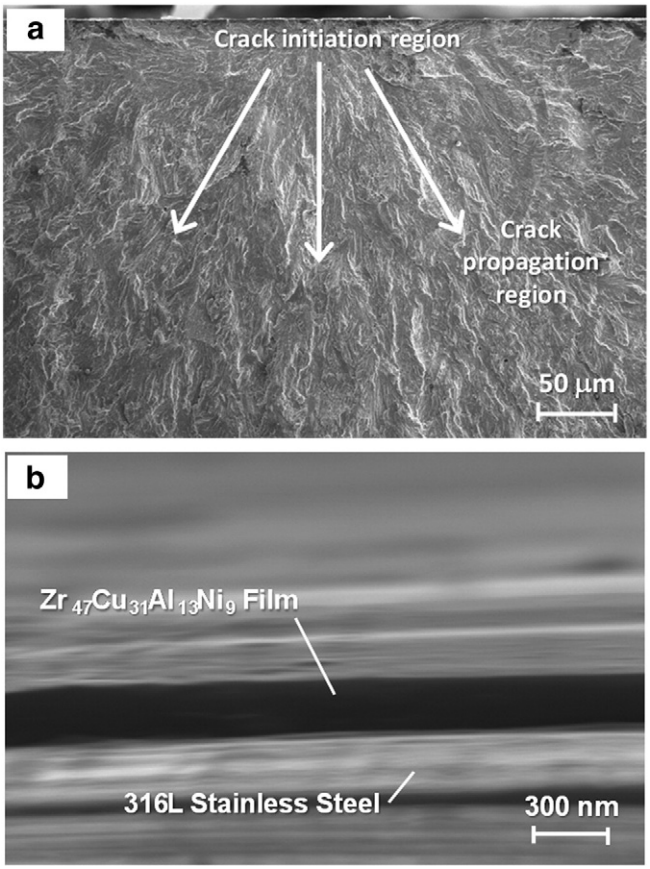

Fig. 37. SEM fractographs of a 316 L stainless steel substrate with a 200 nm-thick $Zr_{47}Al_{13}Cu_{31}Ni_9$ film after a fatigue test to failure: (a) low magnification showing crack initiation and crack-propagation regions, and (b) a titled view [38].

4.5. Microelectronic and optoelectronic applications

There have been very few studies on the evaluation of TFMG optoelectronic properties. Indium tin oxide (ITO), a common transparent electrode has been used extensively in a wide-range of optoelectronic applications, such as liquid crystal displays (LCDs) and scanners. Huang et al. [119] reported performance improvements to conventional ITO by applying a ZrCu-based TFMG to form a bilayer TFMG/ITO transparent conductive electrode on polyethylene-terephthalate (PET) substrates. For comparison, a pure Ag layer was applied to form Ag/ITO. A continuous and smooth film structure was obtained with TFMGs having thicknesses less than 6 nm, in contrast to the undesirable island structure of a pure Ag layer of the same thickness. However, while TFMG/ITO bilayers have optical transmittance of 73% at 550 nm, the specific resistance is relatively high, ~623 Ω/sq, compared to Ag/ITO, ~42 Ω/sq. To decrease the electrical resistivity, proper selection of TFMGs becomes an important issue for this application.

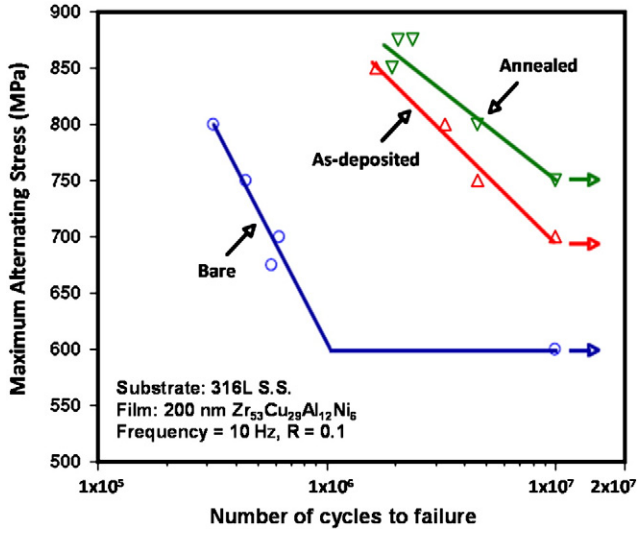

Fig. 38. Fatigue S–N curves of 316 L stainless steel with and without Zr-based TFMGs as-deposited and annealed within ΔT [99]. Arrows indicate run-out data without failure.

A recent study has been carried out to improve stability of the field emission of carbon nanotube (CNT) cathodes by depositing a coating of TFMG [120]. CNT cathodes have been proposed for many applications such as planar light sources, field emission displays, and gas ionization sensors. It is found that the performance of the cathode is greatly improved with a superior long-term stability (lifetime is quadrupled) by applying a thin layer (10 nm) of $Zr_{53}Cu_{29}Al_{12}Ni_6$ TFMG.

Another potential application for TFMGs is the memory device. Nonvolatile memory (NVM) has been widely used in many consumer electronics. Among NVMs, the resistive random access memory (RRAM) is one of the promising candidates for next-generation memory applications, replacing the dynamic random access memory (DRAM) due to excellent retention time, high operation speed, and low power consumption. There are many efforts to find new RRAM materials. Recently, a Zr-based metallic glass oxide film was found to exhibit unipolar (independent of bias voltage polarity) switching behavior, as shown in Fig. 42 [121]. After a forming voltage is applied, the metallic glass oxide film can be reversibly switched between a high resistance state (HRS, set) and a low resistance state (LRS, reset) under low electric stress. In addition, the resistance ratio between HRS and LRS is more than three orders of magnitude, which is large enough for the RRAM application. While further and detailed studies are required to understand the switching mechanism, this result suggests that the metallic glass oxide films may be a new group of materials useful for RRAM devices.

5. Molecular-dynamics (MD) simulations

There is a rich literature on computer simulations of metallic glasses. Molecular-dynamics (MD) simulations have become a general tool for studying deformation mechanisms in materials [122]. An early attempt comparing MD simulations of density-of-states and neutron-scattering with experimental results for $Ca_{67}Mg_{33}$ metallic glass can be found in [123]. Since then, rigorous simulations based on first-principle MD calculations for liquid metals have been intensively performed, such as the one in [124], to overcome deficiencies in empirical interatomic potentials. Configurational energy of glass possesses several nearly evenly spaced potential minima, and hence identifying the correct state requires accurate computational methods. However, the cost for this sort of computation is enormous and only small size models have been explored. Although periodic boundary conditions may reduce this limitation on system size, they cannot help when studies focus on driven dynamics of glassy materials.

In order to simulate large size systems at a given temperature and under a stress state, conventional MD simulation, with empirical interatomic potentials and a chosen statistical ensemble, is usually adopted. Most researchers use rapid cooling in simulation to obtain their initial amorphous models. Improvements of simulation accuracy can be obtained by using experimental data, such as extended X-ray absorption fine structure (EXAFS) radial distribution functions, to refine simulation models with the reverse Monte Carlo method. Once a simulation model is obtained, various mechanical properties can be calculated. For example [125], necking instabilities and shear-band formation in the Mg – Cu system have been studied under uniaxial strain. It is found that the width of the shear band is about 10 nm and temperature increases in the shear band region, along with a slight density drop. Validation of MD

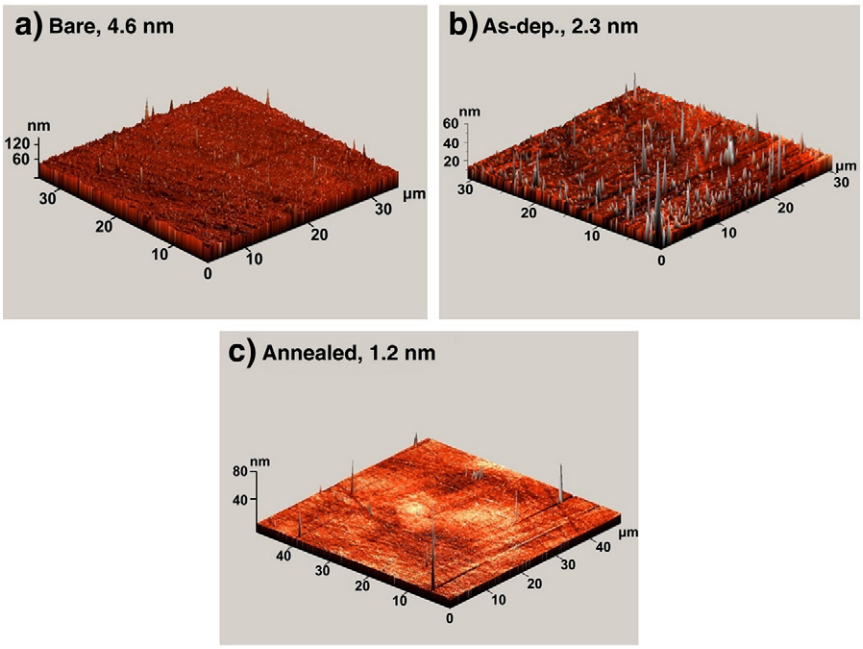

Fig. 39. AFM surface-roughness results for 316 L stainless-steel: (a) as-polished, (b) with an as-deposited 200 nm-thick $Zr_{53}Cu_{29}Al_{12}Ni_6$ TFMG coating, and (c) as in (b) but annealed within ΔT. The numbers in the figure are surface root-mean square roughness values [102].

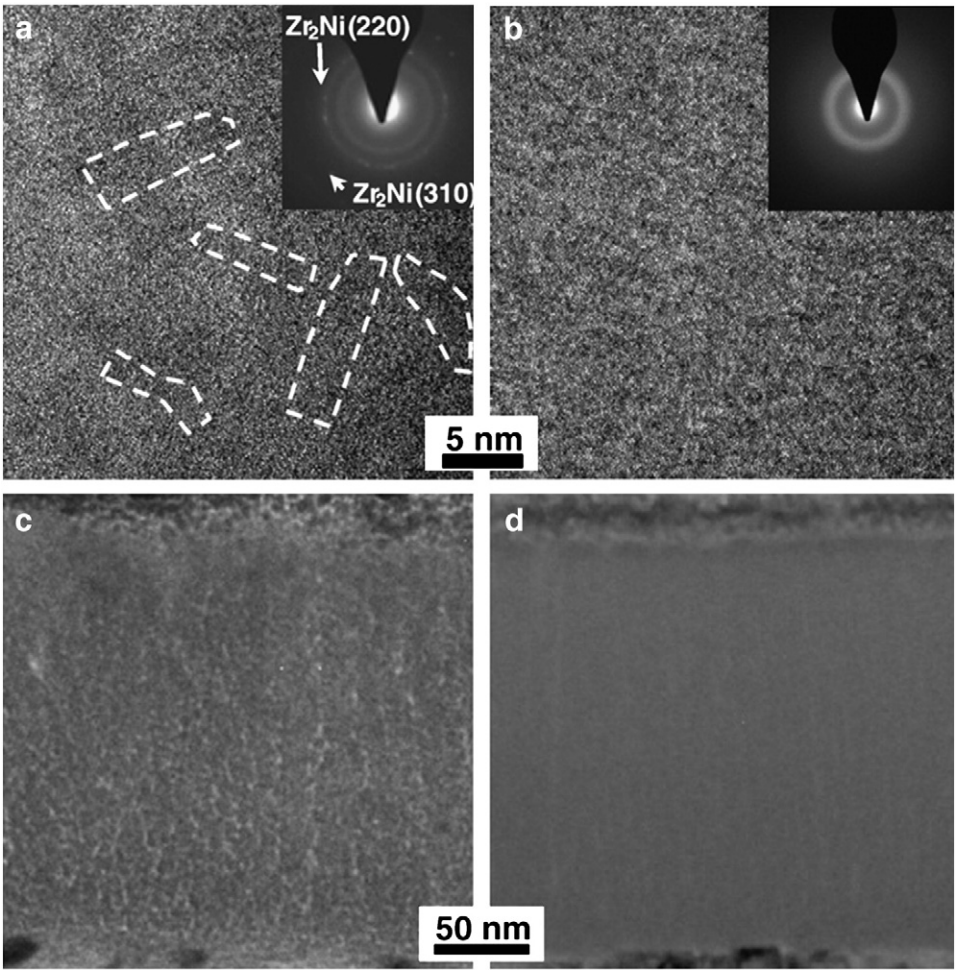

Fig. 40. Cross-sectional TEM images of as-deposited, (a) and (c), and annealed within ΔT, (b) and (d), 200-nm-thick $Zr_{53}Cu_{29}Al_{12}Ni_6$ TFMG/316 L stainless steel samples. Diffraction patterns are shown as insets in (a) and (b). Dotted regions in (a) are short-range order domains present in the amorphous matrix. (c) and (d) reveal columnar microstructures [102].

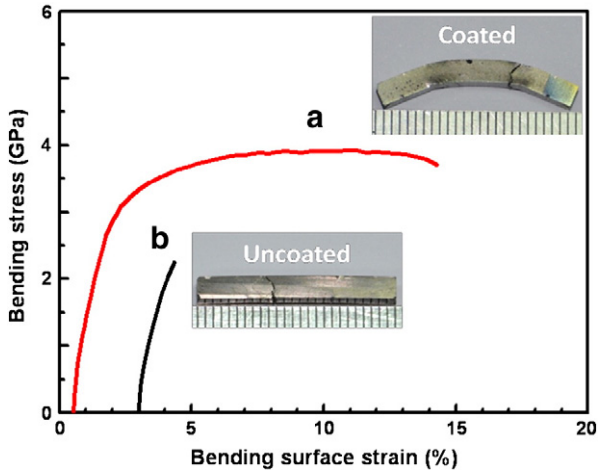

Fig. 41. Bending stress vs. surface strain curves for (a) TFMG/Ti bilayer coated and (b) uncoated BMG samples [84]. The curves are offset along the x axis for ease of viewing. The inset photographs of TFMG/Ti bilayer-coated and uncoated BMG samples are acquired after bending to failure.

simulation results is usually done through comparisons with experimental data. The elastic properties of the Cu–Zr metallic glasses of various compositions have been studied with MD simulations and compared with experimental data obtained by ultrasound techniques, commonly used for measuring elastic properties [126]. Reasonable agreement between simulations and experiments is obtained.

Relatively recently, the medium-range order of metallic glass has been discussed in an attempt to identify structures beyond short-range order [127]. Following similar ideas, the Cu–Zr system has been studied to correlate structure information with mechanical properties, and glass transformation temperature [128]. In addition, power-law scaling and the fractal nature of metallic glasses with medium range order have been explored with MD simulations [129] to probe the self-similar packing of atomic clusters. MD simulations of $Cu_{46}Zr_{54}$ metallic glass have revealed atomic-level structures associated with the glass transformation [130]. The understanding of clustering in disordered systems helps to understand metallic glass structure-property relationships. The connections between local ordering, such as clusters, and the physical properties of metallic glasses are, at the present time, still an intensive research area.

Shear bands are generally known to be the most important deformation mechanisms in metallic glasses. It has been reported that nanocrystallites may form in shear bands produced during severe deformation, a consequence of flow dilatation inside the bands [131]. Shear bands in a BMG, under simple shear, have been studied numerically to determine their critical lengths [132]. The catastrophic critical length is estimated to be 45 μm for $Zr_{65}Al_{10}Ni_{10}Cu_{15}$ metallic glass. However, much smaller shear bands can still exist in the material and cause global fracture. Under pure shear, strain localization of a two-dimensional MD system has been studied [133], and it is found that the strength of the shear transformation zone (STZ) is approximately two to four atomic bonds, consistent with Argon's STZ theory [134]. Further development of STZ theory has been recently proposed, based on MD simulation results [135] for the existence of embryonic shear bands to bridge STZ with fully mature shear bands. Assessments of critical shear band sizes in metallic glasses have been conducted [136], and it is found that the width of shear bands is ~10 to 20 nm. A recent simulation of TFMGs under indentation can be found in [137], showing effective atomic strains are indicative of strain localization under indentation.

Different from rapid cooling or mechanical alloying methods to create amorphous models, MD simulations have also been performed to simulate the sputter-deposition process to create the initial film configuration. During the deposition simulation, the deposited atoms may, depending on their energy level, penetrate into the substrate. A thermal-control-layer-marching algorithm [138] is adopted to reduce computation time for the deposition, while maintaining accuracy. Without the algorithm, the computation for depositing a relatively thick film requires considerably longer time. Fig. 43 shows the results for an as-deposited $Cu_{47}Zr_{47}Al_6$ TFMG. Atoms are represented as small colored circles; Al is red, Cu green, and Zr blue. The substrate is Ti and the film thickness is 80 Å. From this simulation, deposited atoms, are allowed to penetrate into the substrate while forming the TFMG/substrate interface in accordance with the MD code.

In deposition and indentation simulations, interatomic potentials, derived from the many-body tight-binding second-moment approximation (TB-SMA) [139], were adopted to probe the interactions among the three species of atoms forming the metallic glass. The interatomic potentials are expressed as:

$$E_i = -\left\{\sum_j \xi^2 \exp\left[-2q\left(\frac{r_{ij}}{r_0}-1\right)\right]\right\}^{\frac{1}{2}} + \sum_j A\exp\left[-p\left(\frac{r_{ij}}{r_0}-1\right)\right], \qquad (4)$$

where ξ is an effective hopping integer, r_{ij} the distance between atoms, i and j, and r_0 is the first-neighbor distance. The parameters, $A(eV)$, p, q,

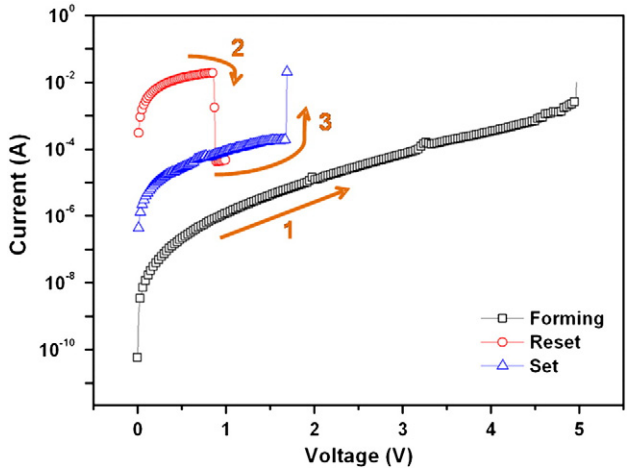

Fig. 42. Typical I–V curves of reversible unipolar switching behavior for a Zr-based metallic glass oxide film on a Pt/Ti/SiO_2/Si(001) substrate. Sequence numbers 1, 2, and 3 indicate the forming, reset, and set processes, respectively [121].

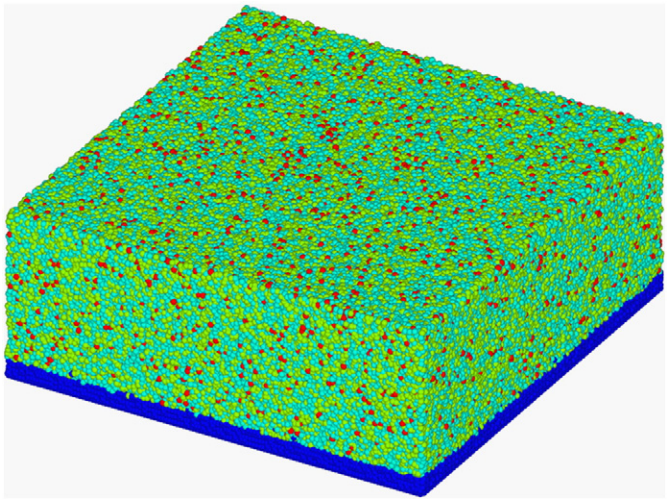

Fig. 43. MD Simulated 80 Å-thick $Cu_{47}Zr_{47}Al_6$ TFMG (Cu atoms = green, Zr = blue, and Al = red) on a Ti substrate.

and ξ(eV) are system-specific parameters. Detailed simulation parameters can be found in [137]. During deposition, the interaction among the working gas, Ar^+, and neutral atoms is governed by the pair-wise Moliére potential, V_{ij} (eV).

$$V_{ij}(r) = \frac{Z_1 Z_2 e^2}{r_{ij}} \left(0.35 \exp\left[\frac{-0.3 r_{ij}}{L_f}\right] + 0.55 \exp\left[\frac{-1.2 r_{ij}}{L_f}\right] + 0.1 \exp\left[\frac{-6 r_{ij}}{L_f}\right] \right), \quad (5)$$

where L_f is the Firsov screening length in Å, and calculated as $L_f = 0.4683 (\sqrt{Z_1} + \sqrt{Z_2})^{-2/3}$, and e is the electron charge. Z_1 and Z_2 are the atomic numbers of the gas ion and neutral atom, respectively.

Fig. 44 shows results for an as-deposited $Cu_{47}Zr_{47}Al_6$ TFMG with an indent at 300 K. In the figure, atoms are color coded according to their engineering strain ε_{11}. Red and blue represent positive and negative strain, respectively. It can be seen that pileup occurs around the indent, indicating homogeneous flow of the metallic glass under an intensive stress around the indenter. In the indentation simulation, interatomic potentials that are derived from the many-body TB-SMA were adopted to simulate the interactions among the four species of atoms after the as-deposited film was indented with a right-angle indenter, the engineering strain ε_{11} under the indent is shown in Fig. 44. No segregation is observed under stress. The displacement loading rate was 166.7 m/s. The atomic strains were calculated from the atom positions as a function of time via a discrete deformation gradient tensor [140]. Radial shear bands (red or blue lines extending from the indents) can be observed. The red/blue regions are of high tension/compression strain, where plastic flow occurs. A larger plastic zone indicates less reaction forces than the zone can provide. Hence, the hardness decreases with loading-rate increases, consistent with experiment [31].

The connection between shear transformation zones (STZs) and atomic shear banding can be understood. At the beginning of the indentation, STZs may be activated at "weak spots" (defined as regions of lower density with atoms loosely packed during deposition) around the indent and embryonic shear bands may form afterwards due to time-dependent properties or continuous loading. With increased loading, embryonic shear bands may propagate, and form mature shear bands. However, the original "weak spots" where shear transformations first took place may become a part of the plastic-flow regions upon further loading. Moreover, during the propagation of shear bands, other "weak spots" in the material may undergo shear transformation when the effective strain reaches a critical value.

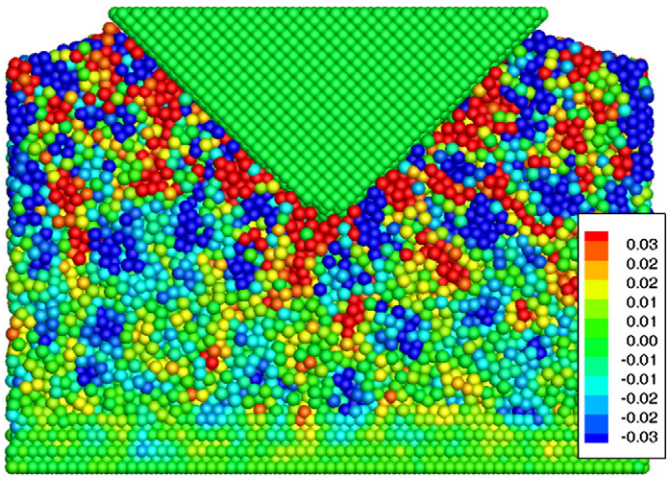

Fig. 44. MD simulation of the engineering strain ε_{11} under a rigid indent in a $Cu_{47}Zr_{47}Al_6$ TFMG on a rigid Ti substrate.

6. Conclusions and outlook

While BMGs are still little used because of their macroscopic brittle nature and the difficulty of processing, TFMGs are a possible solution to take advantage of the unique MG properties of high strength, large plasticity within ΔT, and excellent wear resistance. In this critical review, advantages, disadvantages, and properties of TFMGs are discussed. The latter includes mechanical properties, tribological properties, annealing-induced amorphization and resulting smooth surfaces. Many of these unique properties lead directly to useful mechanical applications. In addition, potential applications in microelectronics and optoelectronics are discussed. Ironically, there have been enormous research efforts dedicated to developing metallic glasses with large critical sizes only to reveal that the most facile use for these materials may, in fact, be in thin film applications. It is, thus, hoped that this review serves the purpose of calling attention to the potential importance of TFMGs as well as the need for more detailed studies.

Acknowledgments

We are indebted to Professor Joe Greene, the Editor-in-Chief, for his critical reading of this manuscript and valuable comments. The authors would like to acknowledge the following financial supports: National Science Council of Taiwan, R.O.C., under NSC-96-2628-E-011-117-MY3 and NSC-98-2221-E-011-037-MY3, U.S. National Science Foundation (NSF), Combined Research-Curriculum Development (CRCD) Program, under EEC-9527527 and EEC-0203415, Integrative Graduate Education and Research Training (IGERT) Program, under DGE-9987548, International Materials Institutes (IMI) Program, under DMR-0231320, Major Research Instrumentation (MRI) Program, under DMR-0421219, the Division of Civil, Mechanical, Manufacture, and Innovation (CMMI) Program, under CMMI-0900271 and CMMI-1100080, and the Materials World Network Program, under DMR-0909037.

References

[1] W. Klement, R.H. Willens, P.O.L. Duwez, Nature 187 (4740) (1960) 869.
[2] H.S. Chen, D. Turnbull, Acta Metall. 17 (8) (1969) 1021.
[3] H.S. Chen, Acta Metall. 22 (12) (1974) 1505.
[4] A. Inoue, A. Takeuchi, Acta Mater. 59 (6) (2011) 2243.
[5] Y.Q. Cheng, E. Ma, Prog. Mater Sci. 56 (4) (2011) 379.
[6] J.F. Löffler, Intermetallics 11 (6) (2003) 529.
[7] C.A. Schuh, T.C. Hufnagel, U. Ramamurty, Acta Mater. 55 (12) (2007) 4067.
[8] W.H. Wang, C. Dong, C.H. Shek, Mater. Sci. Eng., R 44 (2–3) (2004) 45.
[9] L. Tian, Y.-Q. Cheng, Z.-W. Shan, J. Li, C.-C. Wang, X.-D. Han, J. Sun, E. Ma, Nat. Commun. 3 (2012) 609.
[10] J.P. Chu, J.C. Huang, J.S.C. Jang, Y.C. Wang, P.K. Liaw, JOM 62 (4) (2010) 19.
[11] M. Nastasi, F.W. Saris, L.S. Hung, J.W. Mayer, J. Appl. Phys. 58 (8) (1985) 3052.
[12] J. Rivory, J.M. Frigerio, M. Harmelin, A. Quivy, Y. Calvayrac, J. Bigot, Thin Solid Films 89 (3) (1982) 323.
[13] Q.-M. Chen, Y.-D. Fan, H.-D. Li, Mater. Lett. 6 (8–9) (1988) 311.
[14] R.B. Schwarz, W.L. Johnson, Phys. Rev. Lett. 51 (5) (1983) 415.
[15] E.J. Cotts, W.J. Meng, W.L. Johnson, Phys. Rev. Lett. 57 (18) (1986) 2295.
[16] S.B. Newcomb, K.N. Tu, Appl. Phys. Lett. 48 (21) (1986) 1436.
[17] R.J. Highmore, J.E. Evetts, A.L. Greer, R.E. Somekh, Appl. Phys. Lett. 50 (10) (1987) 566.
[18] B.X. Liu, W.S. Lai, Z.J. Zhang, Adv. Phys. 50/3 (2001) 367.
[19] A. Inoue, Acta Mater. 48 (1) (2000) 279.
[20] C.J. Chen, J.C. Huang, H.S. Chou, Y.H. Lai, L.W. Chang, X.H. Du, J.P. Chu, T.G. Nieh, J. Alloys Compd. 483 (1–2) (2009) 337.
[21] H.S. Chou, J.C. Huang, L.W. Chang, Surf. Coat.Technol. 205 (2) (2010) 587.
[22] Y. Li, Q. Guo, J.A. Kalb, C.V. Thompson, Science 322 (5909) (2008) 1816.
[23] S. Hata, K. Sato, A. Shimokohbe, Proc. of SPIE 3892 (1999) 97.
[24] Y. Liu, S. Hata, K. Wada, A. Shimokohbe, Jpn. J. Appl. Phys., Part 1 Regul. Papers Short Notes Rev. Papers 40/9 A (2001) 5382.
[25] P. Sharma, W. Zhang, K. Amiya, H. Kimura, A. Inoue, J. Nanosci. Nanotechnol. 5 (3) (2005) 416.
[26] J.P. Chu, C.T. Liu, T. Mahalingam, S.F. Wang, M.J. O'Keefe, B. Johnson, C.H. Kuo, Phys. Rev. B 69 (11) (2004) 113410.
[27] J.P. Chu, C.-T. Lo, Y.-K. Fang, B.-S. Han, Appl. Phys. Lett. 88 (1) (2006) 012510.
[28] J.P. Chu, JOM 61 (1) (2009) 72.
[29] J.P. Chu, C.-Y. Wang, L.J. Chen, Q. Chen, Surf. Coat.Technol. 205 (8–9) (2011) 2914.
[30] I. Petrov, P.B. Barna, L. Hultman, J.E. Greene, J. Vac. Sci. Technol. A Vac. Surf. Films 21/5 (2003) S117.

[31] G. Kumar, J. Schroers, Appl. Phys. Lett. 92 (3) (2008) 031901.
[32] H.S. Chou, J.C. Huang, L.W. Chang, T.G. Nieh, Appl. Phys. Lett. 93/19 (2008).
[33] M.T. Johnson, et al., Rep. Prog. Phys. 59 (11) (1996) 1409.
[34] D. Sander, Rep. Prog. Phys. 62 (5) (1999) 809.
[35] Y.H. Liu, T. Fujita, A. Hirata, S. Li, H.W. Liu, W. Zhang, A. Inoue, M.W. Chen, Intermetallics 21 (1) (2012) 105.
[36] H.S. Chou, J.C. Huang, Y.H. Lai, L.W. Chang, X.H. Du, J.P. Chu, T.G. Nieh, J. Alloys Compd. 483 (1–2) (2009) 341.
[37] H.S. Chou, X.H. Du, C.J. Lee, J.C. Huang, Intermetallics 19 (7) (2011) 1047.
[38] C.L. Chiang, J.P. Chu, F.X. Liu, P.K. Liaw, R.A. Buchanan, Appl. Phys. Lett. 88/13 (2006).
[39] Y.F. Gao, L. Wang, H. Bei, T.G. Nieh, Acta Mater. 59 (10) (2011) 4159.
[40] F.X. Liu, Y.F. Gao, P.K. Liaw, Metall. Mater. Trans. A 39 (8) (2008) 1862.
[41] W.C. Oliver, G.M. Pharr, J. Mater. Res. 7 (6) (1992) 1564.
[42] B. Bhushan, X. Li, J. Mater. Res. 12 (1) (1997) 54.
[43] R. Saha, W.D. Nix, Acta Mater. 50 (1) (2002) 23.
[44] F.S. Santos, J. Sort, J. Fornell, M.D. Baró, S. Suriñach, C. Bolfarini, W.J. Botta, C.S. Kiminami, J. Non-Cryst. Solids 356 (43) (2010) 2251.
[45] M.A. Hopcroft, W.D. Nix, T.W. Kenny, J. Microelectromech. Syst. 1 (9/2) (2010) 229.
[46] Y. Yang, J.C. Ye, J. Lu, F.X. Liu, P.K. Liaw, Acta Mater. 57 (5) (2009) 1613.
[47] L. Wang, H. Bei, Y.F. Gao, Z.P. Lu, T.G. Nieh, Acta Mater. 59 (7) (2011) 2858.
[48] Y.H. Lai, C.J. Lee, Y.T. Cheng, H.S. Chou, H.M. Chen, X.H. Du, C.I. Chang, J.C. Huang, S.R. Jian, J.S.C. Jang, T.G. Nieh, Scr. Mater. 58 (10) (2008) 890.
[49] C.J. Lee, J.C. Huang, T.G. Nieh, Appl. Phys. Lett. 91/16 (2007).
[50] Z.W. Shan, J. Li, Y.Q. Cheng, A.M. Minor, S.A. Syed Asif, O.L. Warren, E. Ma, Phys. Rev. B: Condens. Matter Phys. 77/15 (2008).
[51] C.A. Volkert, A. Donohue, F. Spaepen, J. Appl. Phys. 103/8 (2008).
[52] J.C. Ye, J. Lu, Y. Yang, P.K. Liaw, Acta Mater. 57 (20) (2009) 6037.
[53] B.E. Schuster, Q. Wei, T.C. Hufnagel, K.T. Ramesh, Acta Mater. 56 (18) (2008) 5091.
[54] M.D. Uchic, P.A. Shade, D.M. Dimiduk, Annu. Rev. Mater. Res. 39 (2009) 361.
[55] D.M. Dimiduk, M.D. Uchic, T.A. Parthasarathy, Acta Mater. 53 (15) (2005) 4065.
[56] M.D. Uchic, D.M. Dimiduk, J.N. Florando, W.D. Nix, Science 305 (5686) (2004) 986.
[57] J.R. Greer, W.C. Oliver, W.D. Nix, Acta Mater. 53 (6) (2005) 1821.
[58] C.E. Packard, C.A. Schuh, Acta Mater. 55 (16) (2007) 5348.
[59] H. Guo, P.F. Yan, Y.B. Wang, J. Tan, Z.F. Zhang, M.L. Sui, E. Ma, Nat. Mater. 6 (10) (2007) 735.
[60] Y. Yang, J. Ye, J. Lu, Y. Gao, P.K. Liaw, JOM 62 (2) (2010) 93.
[61] Y. Yang, J.C. Ye, J. Lu, P.K. Liaw, C.T. Liu, Appl. Phys. Lett. 96 (1) (2010) 011905.
[62] S. Hata, J. Sakurai, A. Shimokohbe, 18th IEEE International Conference on, 2005, MEMS, 2005, p. 479.
[63] G. Kumar, H.X. Tang, J. Schroers, Nature 457 (7231) (2009) 868.
[64] A. Donohue, F. Spaepen, R.G. Hoagland, A. Misra, Appl. Phys. Lett. 91 (24) (2007) 241905.
[65] M.C. Liu, J.C. Huang, H.S. Chou, Y.H. Lai, C.J. Lee, T.G. Nieh, Scr. Mater. 61 (8) (2009) 840.
[66] T.G. Nieh, T.W. Barbee, J. Wadsworth, Scr. Mater. 41 (9) (1999) 929.
[67] Y. Wang, J. Li, A.V. Hamza, T.W. Barbee, Proc. Natl. Acad. Sci. 104/27 (2007) 11155.
[68] M.C. Liu, C.J. Lee, Y.H. Lai, J.C. Huang, Thin Solid Films 518 (24) (2010) 7295.
[69] H.J. Pei, C.J. Lee, X.H. Du, Y.C. Chang, J.C. Huang, Mater. Sci. Eng. A 528 (24) (2011) 7317.
[70] S.Y. Kuan, H.S. Chou, M.C. Liu, X.H. Du, J.C. Huang, Intermetallics 18 (12) (2010) 2453.
[71] P. Sharma, K. Yubuta, H. Kimura, A. Inoue, Phys. Rev. B 80 (2) (2009) 024106.
[72] P.-T. Chiang, G.-J. Chen, S.-R. Jian, Y.-H. Shih, J.S.-C. Jang, C.-H. Lai, Fooyin J. Health Sci. 2 (1) (2010) 12.
[73] F.X. Liu, F.Q. Yang, Y.F. Gao, W.H. Jiang, Y.F. Guan, P.D. Rack, O. Sergic, P.K. Liaw, Surf. Coat.Technol. 203 (22) (2009) 3480.
[74] S.J. Bull, D.S. Rickerby, Surf. Coat.Technol. 42 (2) (1990) 149.
[75] P.J. Burnett, D.S. Rickerby, Thin Solid Films 154 (1–2) (1987) 403.
[76] P.J. Burnett, D.S. Rickerby, Thin Solid Films 157 (2) (1988) 233.
[77] C.T. Pan, T.T. Wu, C.F. Liu, C.Y. Su, W.J. Wang, J.C. Huang, Mater. Sci. Eng. A 527 (9) (2010) 2342.
[78] J.G. Wang, W.B. Choi, T.G. Nieh, C.T. Liu, J. Mater. Res. 15 (2000) 913.
[79] Y. Huang, Y.L. Chiu, J. Shen, Y. Sun, J.J.J. Chen, Intermetallics 18 (5) (2010) 1056.
[80] J.-W. Lee, Y.-C. Kuo, Y.-C. Chang, Surf. Coat.Technol. 201 (7) (2006) 4078.
[81] H. Jehn, G. Reiners, N. Siegel, Charakterisierung Dünner Schichten, Berlin, 1993.
[82] J.-W. Lee, Y.-C. Kuo, C.-J. Wang, L.-C. Chang, K.-T. Liu, Surf. Coat.Technol. 203 (5–7) (2008) 721.
[83] J. Gerth, U. Wiklund, Wear 264 (9–10) (2008) 885.
[84] J.P. Chu, J.E. Greene, J.S.C. Jang, J.C. Huang, Y.-L. Shen, P.K. Liaw, Y. Yokoyama, A. Inoue, T.G. Nieh, Acta Mater. 60 (6–7) (2012) 3226.
[85] M. Ishida, H. Takeda, N. Nishiyama, K. Kita, Y. Shimizu, Y. Saotome, A. Inoue, Mater. Sci. Eng. A 449–451 (2007) 149.
[86] G.Q. Zhang, X.J. Li, M. Shao, L.N. Wang, J.L. Yang, L.P. Gao, L.Y. Chen, C.X. Liu, Mater. Sci. Eng. A 475 (1–2) (2008) 124.
[87] S. Yoon, J. Kim, B.D. Kim, C. Lee, Surf. Coat.Technol. 205 (7) (2010) 1962.
[88] B.T. Jang, S.H. Yi, S.S. Kim, J. Mech. Sci. Technol. 24 (2010) 89.
[89] M. Gerald, L. Mandell, MACP, John E. Bennett, MD, MACP, Raphael Dolin, MD, Principles and Practice of Infectious Diseases, Churchill Livingstone, Philadelphia, 2005.
[90] E.W. Koneman, S.D. Allen, W.M. Janda, P.C. Schrechenberger, W.C. Winn Jr., Color Atlas & Textbook of Diagnostic Microbiology, Lippincott Williams & Wilkins, Philadelphia, 1997.
[91] J.O. Noyce, H. Michels, C.W. Keevil, J. Hosp. Infect. 63 (3) (2006) 289.
[92] L.C. Kuo, C.J. Yu, L.N. Lee, J.L. Wang, H.C. Wang, P.R. Hsueh, P.C. Yang, J. Formos. Med. Assoc. 102/9 (2003) 601.
[93] S.H. Wang, W.H. Sheng, Y.Y. Chang, L.H. Wang, H.C. Lin, M.L. Chen, H.J. Pan, W.J. Ko, S.C. Chang, F.Y. Lin, J. Hosp. Infect. 53 (2) (2003) 97.
[94] Q. Zhao, Surf. Coat.Technol. 185 (2–3) (2004) 199.
[95] H.T. Michels, J.O. Noyce, C.W. Keevil, Lett. Appl. Microbiol. 49 (2) (2009) 191.
[96] J.S.C. Jang, unpublished work, 2011.
[97] J.C. Huang, J.P. Chu, J.S.C. Jang, Intermetallics 17 (12) (2009) 973.
[98] C.T. McCarthy, M. Hussey, M.D. Gilchrist, Eng. Fract. Mech. 74 (14) (2007) 2205.
[99] P.K. Liaw, unpublished work, 2010.
[100] F.X. Liu, P.K. Liaw, W.H. Jiang, C.L. Chiang, Y.F. Gao, Y.F. Guan, J.P. Chu, P.D. Rack, Mater. Sci. Eng. A 468–470 (2007) 246.
[101] J.P. Chu, unpublished work, 2011.
[102] J.P. Chu, C.M. Lee, R.T. Huang, P.K. Liaw, Surf. Coat.Technol. 205 (16) (2011) 4030.
[103] E.S. Puchi-Cabrera, F. Matínez, I. Herrera, J.A. Berríos, S. Dixit, D. Bhat, Surf. Coat.-Technol. 182 (2–3) (2004) 276.
[104] S.X. Song, H. Bei, J. Wadsworth, T.G. Nieh, Intermetallics 16 (6) (2008) 813.
[105] Y.Q. Cheng, E. Ma, Prog. Mater Sci. 56 (4) (2011) 379.
[106] D.C. Hofmann, J.-Y. Suh, A. Wiest, G. Duan, M.-L. Lind, M.D. Demetriou, W.L. Johnson, Nature 451 (7182) (2008) 1085.
[107] S. Pauly, S. Gorantla, G. Wang, U. Kühn, J. Eckert, Nat. Mater. 9 (6) (2010) 473.
[108] W. Chen, K.C. Chan, P. Yu, G. Wang, Mater. Sci. Eng. A 528 (6) (2011) 2988.
[109] J.P. Chu, H. Wijaya, C.W. Wu, T.R. Tsai, C.S. Wei, T.G. Nieh, J. Wadsworth, Appl. Phys. Lett. 90 (3) (2007) 034101.
[110] D.L. Henann, et al., J. Micromech. Microeng. 19 (11) (2009) 115030.
[111] J. Schroers, Adv. Mater. 22 (14) (2010) 1566.
[112] G. Kumar, A. Desai, J. Schroers, Adv. Mater. 23 (4) (2011) 461.
[113] Y.C. Chen, T.R. Tsai, J.P. Chu, H. Sung, J.S.C. Jang, H. Kato, Appl. Phys. Express 5/1 (2012).
[114] S. Hata, T. Kato, T. Fukushige, A. Shimokohbe, Microelectron. Eng. 67–68 (2003) 574.
[115] P. Sharma, N. Kaushik, H. Kimura, Y. Saotome, A. Inoue, Nanotechnology 18/3 (2007).
[116] K. Takenaka, N. Togashi, N. Nishiyama, A. Inoue, Intermetallics 18 (10) (2010) 1969.
[117] K. Takenaka, N. Saidoh, N. Nishiyama, A. Inoue, Nanotechnology 22/10 (2011).
[118] K. Takenaka, N. Togashi, N. Nishiyama, A. Inoue, J. Non-Cryst. Solids 356 (31–32) (2010) 1542.
[119] C.J. Lee, H.K. Lin, S.Y. Sun, J.C. Huang, Appl. Surf. Sci. 257 (1) (2010) 239.
[120] B.R. Huang, T.C. Lin, J.P. Chu, Y.C. Chen, Carbon 50 (4) (2012) 1619.
[121] T.Y. Kao, R.J. Jeng, W.Z. Chang, Y.C. Chen, J.P. Chu, unpublished work, 2012.
[122] A.R. Leach, Molecular modeling: principles and applications, Prentice Hall, 2001.
[123] R.N. Barnett, C.L. Cleveland, U. Landman, Phys. Rev. Lett. 55 (19) (1985) 2035.
[124] G. Kresse, J. Hafner, Phys. Rev. B 47 (1) (1993) 558.
[125] N.P. Bailey, J. Schiøtz, K.W. Jacobsen, Mater. Sci. Eng. A 387–389/0 (2004) 996.
[126] M.I. Mendelev, D.K. Rehbein, R.T. Ott, M.J. Kramer, D.J. Sordelet, J. Appl. Phys. 102/9 (2007).
[127] H.W. Sheng, W.K. Luo, F.M. Alamgir, J.M. Bai, E. Ma, Nature 439 (7075) (2006) 419.
[128] Y.Q. Cheng, H.W. Sheng, E. Ma, Phys. Rev. B Condens. Matter Mater. Phys. 78/1 (2008).
[129] D. Ma, A.D. Stoica, X.L. Wang, Nat. Mater. 8 (1) (2009) 30.
[130] G. Duan, D. Xu, Q. Zhang, G. Zhang, T. Cagin, W.L. Johnson, W.A. Goddard Iii, Phys. Rev. B Condens. Matter Mater. Phys. 71/22 (2005) 1.
[131] J.J. Kim, Y. Choi, S. Suresh, A.S. Argon, Science 295 (5555) (2002) 654.
[132] R. Matsumoto, N. Miyazaki, Scr. Mater. 59 (1) (2008) 107.
[133] Y. Shi, M.B. Katz, H. Li, M.L. Falk, Phys. Rev. Lett. 98/18 (2007).
[134] A.S. Argon, Acta Metall. 27 (1) (1979) 47.
[135] F. Shimizu, S. Ogata, J. Li, Mater. Trans. 48 (11) (2007) 2923.
[136] Q.K. Li, M. Li, Appl. Phys. Lett. 91/23 (2007).
[137] Y.C. Wang, C.Y. Wu, J.P. Chu, P.K. Liaw, Metall. Mater. Trans. A Phys. Metall. Mater. Sci. 4 (1/11) (2010) 3010.
[138] H.C. Lin, J.G. Chang, S.P. Ju, C.C. Hwang, Proc. R. Soc. A Math. Phys. Eng. Sci. 46 (1/2064) (2005) 3977.
[139] F. Cleri, V. Rosato, Phys. Rev. B 48 (1) (1993) 22.
[140] P.M. Gullett, M.F. Horstemeyer, M.I. Baskes, H. Fang, Model. Simul. Mater. Sci. Eng. 16/1 (2008).